Icarus 341 (2020) 113625

Contents lists available at ScienceDirect

Icarus

journal homepage: www.elsevier.com/locate/icarus

Debris accumulations of CO_2 ice in the south polar residual cap of mars: Longevity and processes

P.C. Thomas [a,*], W.M. Calvin [b], P.B. James [c]

[a] Cornell Center for Astrophysics and Planetary Science, Cornell University, Ithaca, NY 14853, United States of America
[b] Department of Geological Sciences, University of Nevada, Reno, NV 89577, United States of America
[c] Space Science Institute, 4750 Walnut Street, Suite 205, Boulder, CO 80301, United States of America

A B S T R A C T

The Residual South Polar Cap (RSPC) of Mars is a thin covering of CO_2 ice resting on water-ice rich deposits. As such, it is a likely indicator of the net effects of recent polar climate. This covering has had minor changes in outline for the period of spacecraft observation (Piqueux and Christensen, 2008a) and estimates of its recent mass balance suggest fractionally small changes in its volume (Thomas et al., 2016). Pit growth by scarp retreat (Malin et al., 2001; Byrne and Ingersoll, 2003a; Thomas et al., 2005, 2013) is a major, relatively easily measured component of the cap's mass balance. This scarp retreat is only the beginning of a process: fracturing, slumping, and sublimation (Byrne et al., 2008; Thomas et al., 2009) lead to production of a trail of debris. This study focuses on that debris using spacecraft imaging data. The rough, relatively dark debris forms ubiquitous ramps, typically tens of m wide, around scarps within pits or on perimeters of mesas. Much wider accumulations of debris, "debris fields," mimic distinctive scalloped outlines of mesas and are observed to originate by merging of expanding pits within a mesa. The subsequent evolution of debris fields includes repeated year-to-year local relief inversions that involve trapping and retention of seasonal ice in low areas that effectively reduce the vertical loss rates. Complete loss of the CO_2 debris from a surface of water-ice rich Polar Layered Deposits (PLD) can initiate new net accumulation of CO_2 ice. The longevity of some debris fields, essentially instances of slow downwasting, appear to facilitate relief inversion on large scales by allowing the surrounding areas to accumulate new CO_2 ice and to thicken relative to the debris fields.

1. Introduction

The Residual South Polar Cap (RSPC) of Mars is a thin (average depth < 5 m) covering of tabular CO_2 ice overlying thicker deposits of water ice and dust (Polar Layered Deposits, PLD), which include significant segregated deposits of CO_2 ice (Phillips et al., 2011; Bierson et al., 2016; Putzig et al., 2018). The first well-resolved images of the cap obtained in 1972 by Mariner 9 revealed diverse morphology and albedo patterns (Murray and Malin, 1973; James et al., 1992); subsequent missions revealed additional morphologic complexity and documented substantial changes from its appearance in 1972. The changes include retreat of pit walls at 2.5–4.5 m/Mars year (Malin et al., 2001; Byrne and Ingersoll, 2003a, 2003b; Thomas et al., 2009), migration of linear trenches in so-called "fingerprint terrain" (Thomas et al., 2016), changes in albedo (James et al., 1992; Becerra et al., 2015; James et al., 2007, 2009, 2010; James and Bonev, 2008), and measurable deposition in some areas (Thomas et al., 2009, 2016). The sizes and expansion rates of pits indicate that some parts of the RSPC are over 100 Mars years old (Thomas et al., 2013). This thin coating of CO_2 ice, covering ~80,000 km^2, represents about 1% of the current mean atmospheric mass (Thomas et al., 2016) while the buried CO_2 deposit is estimated to have a mass roughly equivalent to that of the current atmosphere (Bierson et al., 2016). Mass balance estimates for the RSPC based on morphology suggest there has been little recent net loss or gain because deposition may balance material lost by pit enlargement (Thomas et al., 2016). The outline of the cap at summer minimum extent has changed little over 20+ Mars years (Piqueux and Christensen, 2008a), and atmospheric pressure measurements show any net change in the mass of stored CO_2 is relatively small (Haberle and Kahre, 2010; Kahre and Haberle, 2010; Haberle et al., 2014; Batterson et al., 2017).

Although the RSPC's mass may be nearly stable, erosion of pits and troughs by scarp retreat is obvious, ubiquitous, and continuing (Malin et al., 2001; Byrne and Ingersoll, 2003b). This scarp retreat is not simple sublimation of a steep wall of ice, rather it includes fracturing, slumping, block rotation, and sublimation (Byrne et al., 2008; Thomas et al., 2009; Buhler et al., 2017) and usually produces rough, relatively dark accumulations that follow the retreat of the scarp, be it within pits in extensive layers or bounding isolated mesas. We term these accumulations "debris ramps" and they are integral parts of scarps in all areas of the RSPC. There are wider areas of rough debris previously termed "collapse" or "downwasting" (Thomas et al., 2005) but here we term them "debris fields." These areas of rough debris accumulation might be

* Corresponding author.
E-mail address: pct2@cornell.edu (P.C. Thomas).

https://doi.org/10.1016/j.icarus.2020.113625
Received 8 June 2019; Received in revised form 11 December 2019; Accepted 6 January 2020
Available online 11 January 2020

treated as extraneous details in the erosion of the RSPC were it not for their distinctive relatively low albedo, their longevity (in some cases at least 24 Mars years), and by their association with examples of inversion of relief.

This work explores some characteristics and ramifications of these debris accumulations. We first summarize the data, methods, and usage before examining the basic characteristics of debris and the different but related generation of debris ramps and debris fields. We then examine the late stage evolution of debris fields which includes the phenomenon of repeated, small-scale inversions of relief. We compare photometric data from CTX data to seasonal milestones identified in HiRISE data, followed by discussion of possible mechanics and significance of debris evolution. Supplemental material includes background information as well as specific documentation of the Figures and data used in the text.

2. Data, methods, and usage

This study is primarily based on data from Mars Reconnaissance Orbiter's Context Imager (CTX) and High Resolution Imaging Science Experiment (HiRISE) (Malin et al., 2007; McEwen et al., 2007) and the Mars Observer Camera (MOC) on Mars Global Surveyor (Malin et al., 1992). This paper takes advantage of the ten Mars years of scattered high resolution imaging of the RSPC (1.5 m/pixel Mars years 24–28; 0.25–0.5 m/pixel MY28–33), and six Mars years of complete spring and summer CTX coverage at 6 m/pixel.

Data are used in map projection, reliant upon topographic data from the Mars Orbiter Laser Altimeter (MOLA), which do not extend poleward of 87°S (Smith et al., 2003). Comparisons of near-nadir images suffer little from projection errors of topography; some projections using interpolated topographic data south of 87°S are affected by the higher emission angles, but most of our photometric work is within the area of MOLA coverage. Seasonal and year-to-year comparisons of CTX data rely upon registering common features such as pit centers, polygonal trough intersections, and small knobs. This registration is usually good to one CTX pixel over the areas sampled. HiRISE registrations use crack intersections, knobs, and small pits. Shadow measurements are used to find heights of scarps, ridges, and depths of troughs. These measurements are made from MOC and HiRISE images with incidence angles generally between 70° and 80° and pixel scales of 0.25–1.5 m. High incidence angles can provide longer shadows, but atmospheric scattering often makes these shadows indistinct. The season of observation also affects the ability to measure shadows because albedo contrasts can confuse shadow patterns; measurements obtained during periods of seasonal ice can be useful even if shadows are somewhat shorter, with the caveat that the measured relief includes remaining portions of seasonal ice. The figures display only portions of the referenced images. Figures referencing the Mars year 33 summer mosaic use data obtained between Ls 324° and Ls 345°.

We use the solar longitude of Mars (L_s) to designate the season: 0° is the start of northern spring; 270° is the start of southern summer. Our map coordinates are Aerographic; these use West longitudes (Archinal et al., 2011). We use "MY" to denote a particular Mars year and "♂y" to denote intervals of Mars years. MY 1 started in April 1955 (Clancy et al., 2000; Piqueux et al., 2015).

We refer to all forms of solid CO_2 as "ice" without any implications for its formation process, porosity, or crystalline nature.

We use approximate Lambert albedos derived from the CTX data for temporal photometric comparisons; these data are uncorrected for atmospheric effects. Designation of individual photometric sampling areas is by region, such as R14, and area, such as 2, in the format: Region_number, e.g. "R14_2." We retain our original working region numbers, far more numerous than dealt with in this work, to reduce chances of author confusion. Error bars report one standard deviation of the sampled data.

This paper refers to several previous works including the first author, which are abbreviated as follows: Thomas et al., 2000: T2000; Thomas et al., 2005: T2005; Thomas et al., 2009: T2009; Thomas et al., 2013: T2013; Thomas et al., 2016: T2016.

We refer to distinct materials underlying the RSPC as "PLD." These materials are distinguished from the CO_2 ice by their polygonal trough or polygonal fracture patterns (Phillips et al., 2011; Bierson et al., 2016), by their stability compared to adjacent CO_2 ice, by their relatively low visible albedo, and at large scales, by their summer time temperatures (e.g., Piqueux et al., 2008). While these materials are likely H_2O-ice rich deposits, the stratigraphy and makeup of materials underlying the surficial CO_2 ice is not settled. A significant complicating factor in assigning these distinct surfaces to the PLD is the presence of H_2O-ice bounding layers within the buried CO_2 detected by the Shallow Radar (SHARAD) on Mars Reconnaissance Orbiter deposits (Bierson et al., 2016; Putzig et al., 2018). There is also a top H_2O-ice bounding layer at or near the surface. The two bounding layers at depth are unconformable with PLD layering; the top layer may be conformable with the PLD layers (Bierson et al., 2016, Fig. 2). It is not known how this top layer relates to the materials and history of the main construct of the PLD, thus there is uncertainty in assigning any distinct surface below the RSPC to the PLD. Additionally, Tanaka et al. (2007) mapped the southern residual ice cap as Planum Australe 4 unit (Aa4) as lower and upper members, Aa4a (lower, H_20 ice) and Aa4b (upper, CO_2 ice). For brevity and convenience, in this work we use "PLD" to signify all PLD and PLD-like materials that underlie the RSPC CO_2 layers.

3. Some terms

We summarize RSPC-specific terms used extensively in this paper; some are modifications of published work.

A unit: The thickest units of the RSPC. See T2016 for full unit descriptions.

A0: The thickest unit, ~10 m thick, with nearly circular depressions commonly several hundred m in diameter; polygonal troughs and ridges occur on upper surfaces.

A1: About 8–10 m thick, with asymmetric, heart-shaped depressions, debris ramps less prominent than on A0.

B units: Thinner units covering >50% of the present RSPC, generally <3 m thick, some of which have been documented as post-MY 9 deposits, that is, after Mariner 9 observations in 1972.

Incipient pit: Depressions on upper surfaces of RSPC layers, generally <12 m across, with rounded profiles, that is, lacking distinct scarp edges.

Reticulated surface: A or B unit surfaces with dense covering of small pits; The A0 occurrences have repeating, crossing, linear patterns.

Debris ramp: Rough, ridged, vermiform (worm-like, narrow, sinuous patterns) topography extending from eroding scarps, generally darker than surrounding flat areas in late summer, typically 20–80 m wide at A unit scarps; up to 20 m wide at B unit scarps. (Fig.1).

Debris field: Rough, ridged topography, distinguished from ramps by greater size, and by nested, rounded depressions that control local ridge patterns. Darker than surrounding flat areas in summer. Some merge with ramps from surviving A0 materials. Debris fields mostly occur with scalloped shapes mimicking outlines of A0 mesas. (Fig. 1).

Senescent debris field: Debris field, usually having typical scalloped outline, but largely lacking identifiable nested depressions and well-developed vermiform ridge patterns; likely <2 m thick.

Debris field pits: Individual or nested depressions within debris fields, usually with rounded crests between nested examples and in late summer displaying vermiform topography and albedo patterns.

Fossil relief inversion: Inversion of relief inferred from preservation of a topographic plan shape distinct to positive relief forms, but is now lower than surroundings.

Contemporary relief inversion: Changing of relative relief observed in time series of images.

Wind-cleared features: Tapered windows in the B units associated with mesas of either B or A unit materials. Generally <1 km in length.

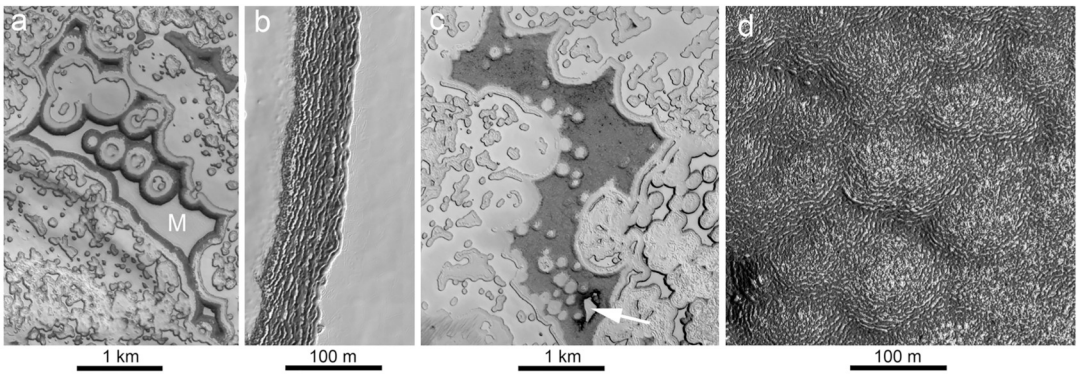

Fig. 1. Debris ramps and debris fields. (a) Mesas of A0 materials (M) with flanking dark debris ramps. 85.48°S, 69.91°W, CTX MY 33 summer mosaic. (b) HiRISE view of debris ramp, 86.78°S, 344.26°W, ESP_32535_0930_RED, MY 31, Ls 346.8°. Top of mesa is on right side. (c) Debris field mimicking a previous mesa outline including one small remnant mesa (arrow), 84.14°S, 56.19°W; MY 33, CTX summer mosaic. (d) Debris field material with pits (10's m scale) and ridge and trough structures (m scale) that produce vermiform patterns; 86.32°S, 0.58°W, HiRISE image PSP_ 5728_0935_RED, MY 28, Ls 331.9°.

They are darker than B and A units and appear to expose the PLD materials. See T2005, Sec. 8.5, and Fig. 15d in T2009.

4. Debris ramps and debris fields: characteristics and origins

4.1. Basics

As previously noted, scarp retreat in the RSPC is not simply sublimation removal of a steep wall. The fracturing attendant to scarp retreat generates rough debris that flanks essentially all pit and mesa walls (Fig. 1a, b), regardless of scarp height. We term these forms "debris ramps." The fracturing that drives scarp retreat results in repetitive ridges and troughs, approximately parallel to the scarps, and which can include bright and dark albedo "tuning-fork" patterns. During much of the summer season the debris ramps display strong albedo contrasts between ridge and trough surfaces (Fig. 1b) as well as shadowing that emphasizes the lineated, but complex topography of the ramps.

Similarly rough, complex, and relatively dark topography exists in patches of various shapes that are much larger than the typical ramps. These areas of debris were previously mapped as "collapsed" material (T2016) to distinguish them from what might be debris left by normal scarp retreat (T2005; esp. Fig. 20). Here we use "debris field" to denote wide areas of debris (minimum widths typically >500 m) that cannot be attributed to simple scarp retreat. Debris fields usually display scalloped margins (Fig. 1c) and merging depressions (Fig. 1d), termed "debris field pits," that show vermiform patterns of ridges and troughs.

4.2. Characteristics of debris ramps

Typical debris ramps abutting A0 material are shown in Fig. 1 with similar scale views of debris fields. Ramps have previously been discussed and illustrated in some detail in T2000 Fig. 2c and d; T2005 Figs. 5f, g, h, and 19; T2009 Figs. 4b, 7, and 10. For A0 and A1 units the ramps are ubiquitous. Debris ramps are common for B units, but their small widths restrict documentation of their details to MOC or HiRISE images. We have sampled A unit ramp widths in widely scattered locales in CTX and HiRISE data (Fig. 2); the CTX data have a wider geographic range than do the HiRISE data. The distributions of CTX and HiRISE widths are slightly different, but both have a tail extending 50–70 m wider than their modal values. We also sampled widths in the same locations in both CTX and HiRISE images (G14_023821_0944_XN_85S074W_110826 and ESP_023821_0945_RED, respectively) near 86°S, 0°W to check the reliability of these measurements in CTX data, where they are typically only a few pixels across. In these samples the CTX mean width is 63.1 ± 10.0 m; for HiRISE it is 60.4 ± 12.1 m. Thus ramp widths in A unit materials have a modal value of 20–30 m, with a significant tail extending ~60 m further.

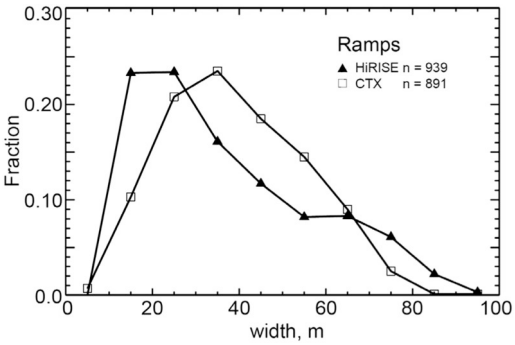

Fig. 2. Widths of debris ramps on A-unit mesas. Measurements in scattered locations across the RSPC from CTX MY 33 summer mosaics at 6 m/pixel and from HiRISE images at 0.25–0.5 m/pixel. Widths are single line measurements perpendicular to mesa scarps at tops of the ramps to the farthest exposure of contiguous dark/rough ramp material (excludes small outliers).

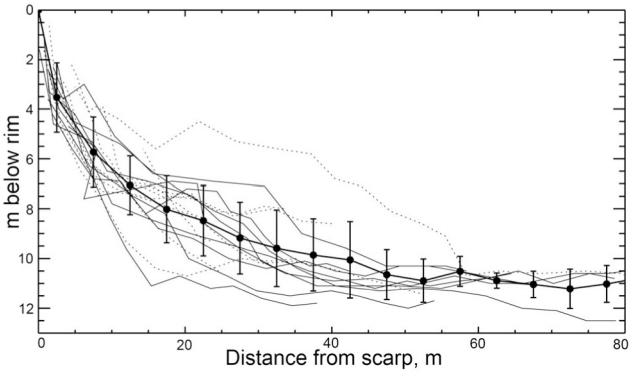

Fig. 3. Profiles of ramps in A-unit materials calculated from shadow measurements. Vertical axis is depth of shadow point below upper surface; the horizontal axis is the shortest distance of that shadow point to the scarp edge. Measurement geometry is shown in Fig. S1. Solid, light lines are all from PSP_003239_0875_RED at 87.8°S, 16.2°W. The dashed lines are from the following areas: ESP_020736_RED, 86.9°S, 60.9°W; ESP_038324_RED, 86.3°S, 0.77°W; ESP_038300_RED, 85.7°S, 75.5°W; ESP_041174_RED, 84.3°S, 58.4°W. Heavy solid line with data points is the mean profile in 5–m bins of distance from scarp. Error bars are one standard deviation of heights in each bin.

We made height profiles of several ramps based on unusual circumstances (Fig. S1) of solar incidence and azimuth relative to A unit scarps that allow shadow measurement sampling across ramps (Fig. 3). These measurements depend upon the assumption of a level scarp edge that casts a shadow on the ramp materials. The rough ramp topography itself can cast shadows, so the points measured tend to be on the higher parts of the local ramp topography. The trace of the shadow also is not perpendicular to the scarp (Fig. S1), so distances to the scarp from shadow points do not follow a single straight profile line. These profiles are rough, generally concave-up, and usually extend <50 m, but can exceed 80 m (consistent with the samples in Fig. 2a). With scarp retreat rates of ~ 4 m/♂y (T2013; T2016), these profiles record the gradual loss of the rough debris over ~10 to 25 ♂y. Crudely, the ramp height decreases by 8 m in the first 20 m distance, an inferred period of ~5 ♂y. Over the next 5 ♂y, represented by ~20 m additional distance, the average height is reduced two additional meters. Beyond 10 ♂y, ~40 m distance, heights change more slowly. Examples of photoclinometric profiles of A0 and B unit ramps, obtained in spring with seasonal frost cover, are given in T2009, Fig. 21. These profiles show the fine structure of the ridges and troughs that cannot be derived from the scarp shadow profiles in Fig. 3.

4.3. Characteristics of debris fields

Example images of debris fields in CTX data are given in Fig. 4. Debris fields found in the MY 33 summer CTX coverage are mapped in Fig. 5. The debris fields occur in essentially all parts of the RSPC except areas with linear depressions (fingerprint terrain, T2016), and in some areas of thin B unit cover (far left of Fig. 5). Debris fields occur 2 to 4.7 km above datum with little concentration in elevation (good elevation data are restricted to areas north of 87°S). Debris fields have been mapped in the CTX summer data on the basis of occurrences of relatively dark, rough areas with distinct margins; most are identifiable as outlines of former A0 mesas by their scalloped edges with arcs 100's of m in radius. Many debris fields lack any surviving remnant of A0 or other precursor mesas (Fig. 4a, b); others are contiguous with mesas and surrounding ramps (other Fig. 4 panels).

Although the thinner B units can leave debris ramps (T2009, Figs. 6 and 21), their widths of only a few m quickly distinguish them from the A unit debris fields. The vast majority of the mapped occurrences in Fig. 5 are from erosion of A0 mesas. The cumulative area of the debris fields is ~70 km^2. This value compares with the present (MY31) area of A0 materials of about 280 km^2 (T2016).

The rough topography in debris fields commonly has a polygonal appearance from the presence of crudely equidimensional, nested depressions (the debris field pits; Figs. 1d, 4e). The ridges between these depressions usually have rounded crests and thus can be ill-defined. In summer, the ridge and trough morphology and common presence of brighter ice in troughs in the debris pits results in vermiform albedo markings a few m wide, and up to tens of m in length. These patterns run crudely parallel to the debris pit crests, but are less organized in the floors of the pits. Most identifiable debris field pits are only a few tens of m across (90% are smaller than 135 m), but the largest reach 250 m (Fig. 6, and Table S1). Because of the nested arrangement of the pits, the year-to-year appearance of debris fields does not change dramatically except for differences in the amounts of brighter ice covering.

Qualitatively, there is no sharp distinction between morphologies within debris ramps and the wider debris fields (Figs. 1, 4). The basic pattern of ridges and troughs in the debris field wrap around the different sides of adjacent mesas and do not show obvious discontinuities from the wider debris field (Fig. S2). Quantitatively, measurements of scarp retreat on A0 mesas adjoining debris fields give averages of 4.1 ± 0.6 m/♂y, a value indistinguishable from the previous wider study of A0 retreat rates of 4.4 m/♂y (T2013). These measurements are summarized in Supplemental Section 1, Fig. S2 and Table S2.

Some debris fields lack the pattern of nested depressions and vermiform patterns of albedo and topography, but can be identified by their outlines inherited from distinctive A0 topography and by their relatively low albedo (Fig. 1c). These debris fields appear to be thin, under 2 m from minimal shadowing and comparisons to nearby B unit layers (See Sec. 5). Although they are typically darker than their surroundings, in some instances their albedos are higher than those of most other debris fields. These debris fields are termed "senescent", as they appear to be a late stage of degradation of the initially thicker, rougher debris.

4.4. Debris field origin: past development

Long term study of debris field development (that is, extending prior to MY 24) is limited to the ~30% of the cap usefully imaged at ~90 m/pixel by Mariner 9 in late southern summer of MY 9. One area of interest emerged because a bright area visible in MY 9 shrank to a small mesa in MY 28 (T2009, Figs. 10 and 15). This feature at ~86°S, 0°W is the best example of loss of a mesa far more rapidly than is explainable by current scarp retreat rates. This feature borders on an elongate dark feature termed the "Tooth" (James et al., 2009; part of HiRISE target "Trujillo"); Fig. 7 shows a key to the Tooth's changes. Another, but less obvious example of loss of a bright mesa is shown in Fig. S3. We have measured six examples of ostensibly unusually rapid loss of A unit mesas (Figs. 7 and S3) to estimate the implied minimum scarp retreat rates between MY 9 and MY 33. Rate results range from 6.8 m/y to 31 m/♂y for the Tooth and the region in Fig. S3, and are summarized in Table 1. These rates are only approximate for two reasons: First, the MY 9 images are at

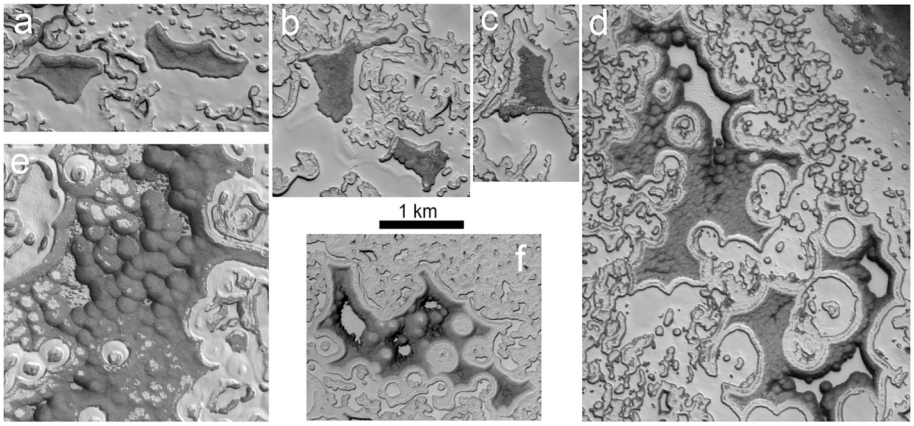

Fig. 4. Debris fields. (a) 88.13°S, 15.87°W. (b) 86.56°S, 77.09°W. (c) 86.42°S, 74.77°W. (d) 87.93°S, 84.80°W. (e) 87.69°S, 359.14°W. (f) 83.89°S, 55.89°W. All panels are from Mars year 33 summer CTX images.

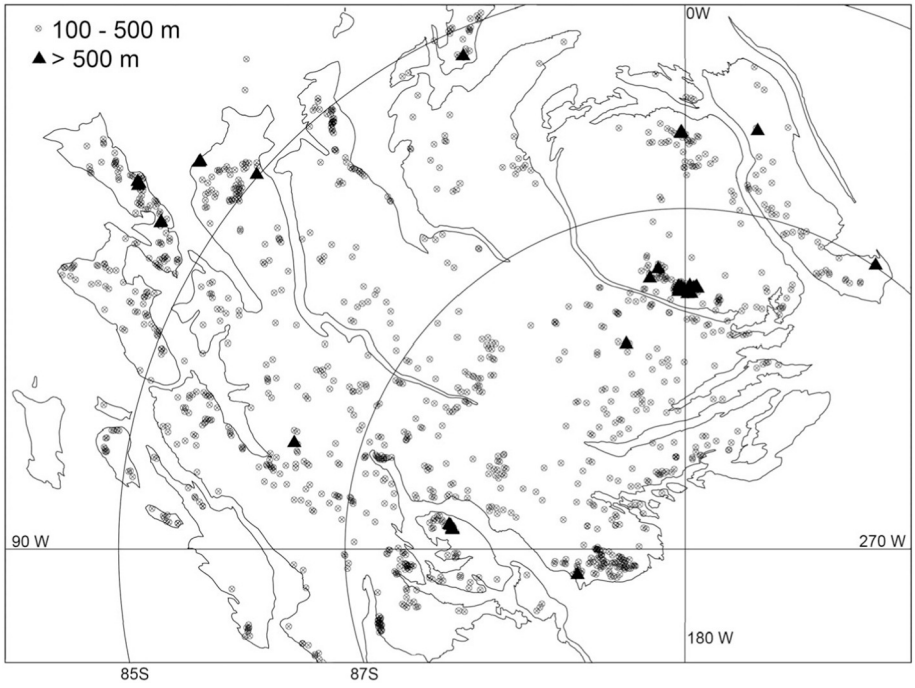

Fig. 5. Debris field occurrences mapped from CTX data. Symbols separate smaller and larger fields. These are approximate measures because of the irregular shapes.

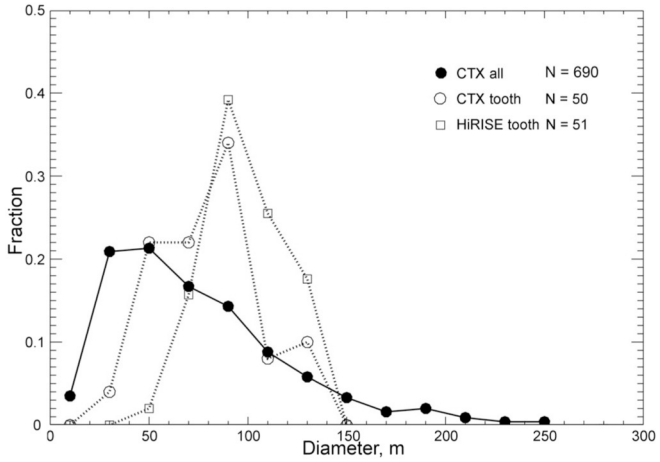

Fig. 6. Widths of debris field pits. Closed symbols are for all debris field pits marked in the MY 33 CTX summer mosaic. Open and closed symbols compare measurements in the debris fields that are part of the feature informally called the "Tooth" (Fig. 7). While many of these nested depressions are approximately equidimensional, some are noticeably longer in some directions; see Figs. 1d and 4. Measurements attempt to record average widths.

~90 m pixel, and are vidicon data that make for sub-optimal comparisons with the later, higher resolution CCD data. Second, the appropriate interval during which the change occurred is not well constrained. The calculated scarp retreat rates in Table 1 include one that is 7 times the average scarp retreat rates for unit A0, two are roughly twice the average rate, and others are within a factor of two of expected rates. Only the highest value, for the "Tooth"at over 30 m/♂y, previously noted for its likely "collapse" (T2009), unequivocally calls for a process beyond simple scarp retreat from the previous perimeter of the mesa, although the remainder would qualify if shorter intervals apply.

While measureable examples of rapid loss of mesas after MY 9 are scarce, preserved examples of the distinctive A0 mesa shapes are common. The combination of the preserved plan shapes of A0 mesas by the debris fields and the presence of nested depressions (Fig. 1d) show that one continuous scarp has not swept inward from an initial perimeter over each debris field, but rather multiple centers of erosion have been involved in forming the debris fields. The preservation of nearly circular arc segments inherited from former mesa scarps means that the entire lengths of the scarps ceased retreating at about the same time.

4.5. Debris field origin: contemporary development

The presence of nested depressions in debris fields prompted a search for occurrences of precursor small, closely spaced pits in A0 and B mesas. An occurrence in A0 material was indeed found in the CTX data (by PBJ; Fig. 8). We term the features in Fig. 8 "reticulated surfaces," emphasizing the role of repeating, crossing, linear patterns (Moore and Wilhelms, 2001), but also inspired by analogy to some terrestrial nomenclature. We map sites of reticulated surfaces in Fig. 9 along with those of pits in debris fields. Many of the reticulated surfaces are in the thinner B units, some of which are shown in Fig. S4. These B unit examples may not follow the same evolutionary paths as in A units, and we do not pursue the B unit debris development in detail. The A unit occurrences of reticulated surfaces are scattered widely as are the A unit outcrops. Whatever process generates the reticulated surfaces occurs at a wide range of altitudes, latitudes, longitudes, and layer thicknesses, but at any one time it constitutes a tiny fraction of the area of the RSPC (the symbols in Fig. 9 are larger than the sizes of the local coverage by the reticulated pits).

Fig. 8 shows that in a five ♂y interval, the slightly pitted surface of this A0 mesa largely converts to a typical debris field. The pits start as subtle depressions with indistinct margins, <15 m across, and usually with some linear floor topography (Figs. 8g–j; Figs. S7, S8). Some incipient pits have crossing patterns of lineations within their small floor areas. The edges of these depressions larger than 10 m usually have distinct scarps and ostensibly expand in the manner as do other RSPC scarps. This expansion leaves alternating ridge and trough topography roughly parallel to the outer scarp edge.

The qualitative evolution of pits shown in Fig. 8 is quantified in Fig. S6 and Table S3. The mesa scarps retreat at 4.7 ± 0.4 m/y; the expanding pits average only 2.4 ± 0.6 m/♂y. However, Figs. 8 and S7 show that for

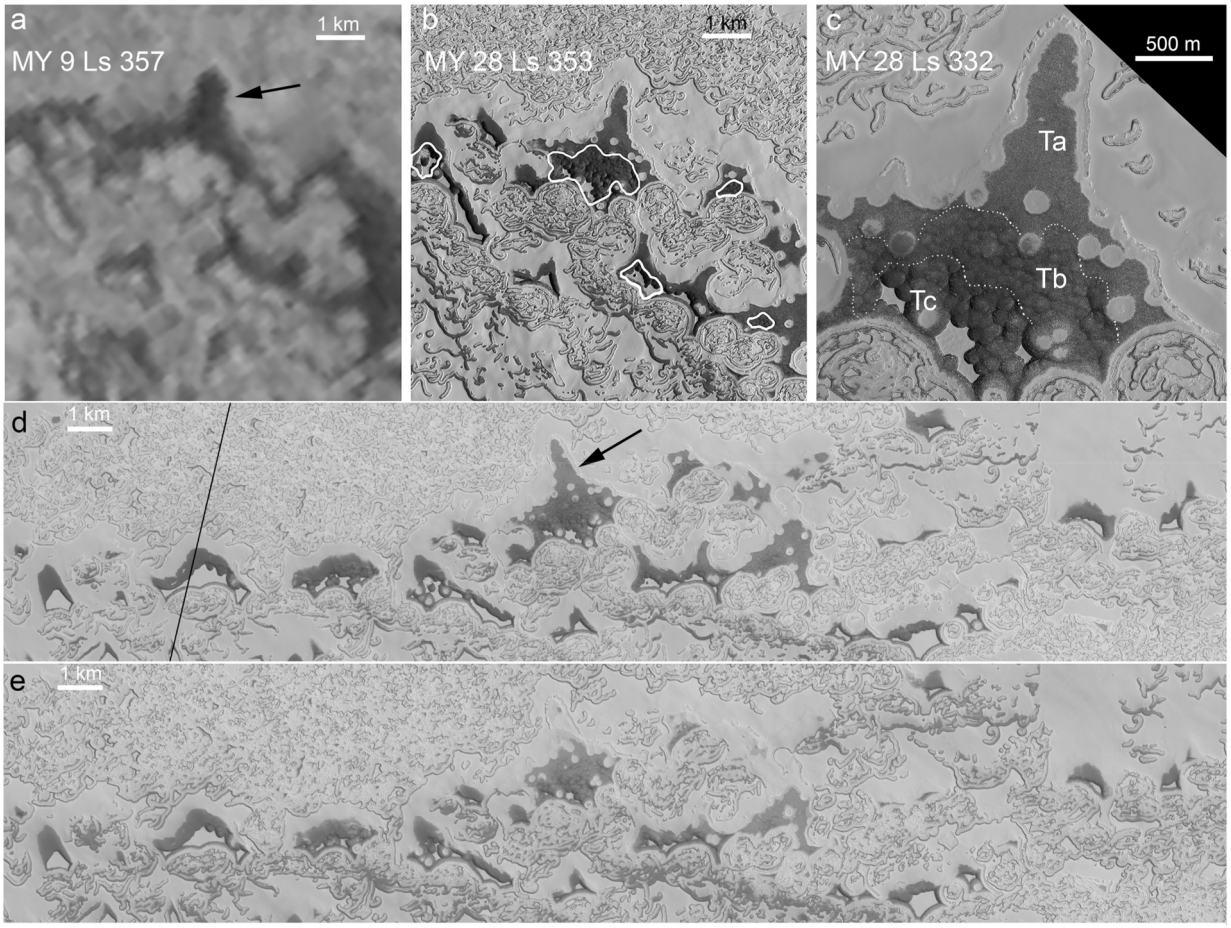

Fig. 7. The "Tooth"and surroundings showing loss of A0 mesa after MY 9 and its regional context. (a) Mariner 9 image 231b01, 86.31°S,0.61°W, MY 9, Ls 357°. Arrow identifies the Tooth. (b) Same area as (a) with outlines of inferred MY 9 mesas. CTX image P06229_0951_XN_84S_014W_071124, MY 28, Ls 353°. (c) Regions of the Tooth. HiRISE image PSP_ 5728_0935_RED, MY 28, Ls 332°. (d) CTX view of Tooth region, MY 28. The Tooth, arrow in upper middle, has a slightly different orientation from views in panels "a" to "c." Wind-cleared regions taper from several of the A0 mesas. Image P12_005728_0938_XI_86S002W_071016; Ls 331.9°. Line near left is image is from dropped lines in original image. (e) CTX image J13_049836_0931_XN_86S349W_170314, MY 33, Ls 333.0°. Same region as panel "d." Note changes in the Tooth (black arrow) and other, but less prominent, changes.

Table 1
Model retreat rates for mesas eroded post –MY9.

Initial	Last	Interval	Width	Rate	Lat	Long
		♂y	m	m/♂y	°S	° W
MY 9	MY 33	24	250	10	84.3	58.6
MY 9	MY 28	19	590	31	86.3	0.61
MY 9	MY 28	19	180	9.5	86.3	359.9
MY 9	MY 28	19	130	6.8	86.4	359.8
MY 9	MY 28	19	160	8.4	86.3	0.41
MY 24	MY 33	9	70	7.8	86.3	0.61

Width is distance scarp would have to retreat. Rate is simply width/interval.

the initial one to two Mars years of data the expansion rate of small, smooth-crested, incipient pits is much slower. After the pits acquire definite scarps their retreat rate is ~3.2 m/♂y. This change is reflected in the substantial difference in appearance between MY 30 and MY 33 shown in Fig. S7. Measurement of scarp retreat rates has shown a positive correlation between scarp height and retreat rate: higher scarps translate more quickly (T2005; T2016). Thus, on a crude level these pit edges behave similarly to other pit scarps. Most of the measurements of the smaller scarps in T2016 were of thin B unit materials overlying (most likely) PLD materials. In this A0 mesa, the small pit scarps overlie lower portions of the CO_2 mesa, and thus their mechanics of retreat may not be fully comparable to those of scarps of B materials that directly overly the PLD. Once the incipient pits on the mesa's upper surface establish distinct retreating scarps, their changes are well within the norms of other pits in the RSPC.

What initiates the pits that evolve to reticulated surfaces? In this area of the RSPC and the observation time interval, no new examples of what we term incipient pits are seen to form. All of the incipient pits show lineations on their floors, some show just one dominant set, others show two directions of lineations (top of Fig. 8g; Fig. S8). Lineations on the floors of the incipient pits are usually expressed as ridges, with spacing of ~ 1.5–2 m. Lineations outside the pits on the mesa surface are more subtle, though they have widths similar to those within the pits. Fig. 8 and Figs. S7 and S8 suggest, unsurprisingly, a role for structures such as fractures, being involved in pit formation, as noted in works such as Buhler et al. (2017). As with most natural phenomena, exact limits on appearances and behaviors are rare, and with loss of mesas to form debris there are variations on the sequence shown in Fig. 8. Two examples of what might be regarded as intermediate between simple scarp retreat and the expansion of separate pits are shown in Fig. S9.

4.6. Summary of characteristics of debris ramps and debris fields

- Scarp retreat in pits and along mesa perimeters is ubiquitous in the RSPC and leaves behind ramps of relatively dark, rough CO_2 ice debris.

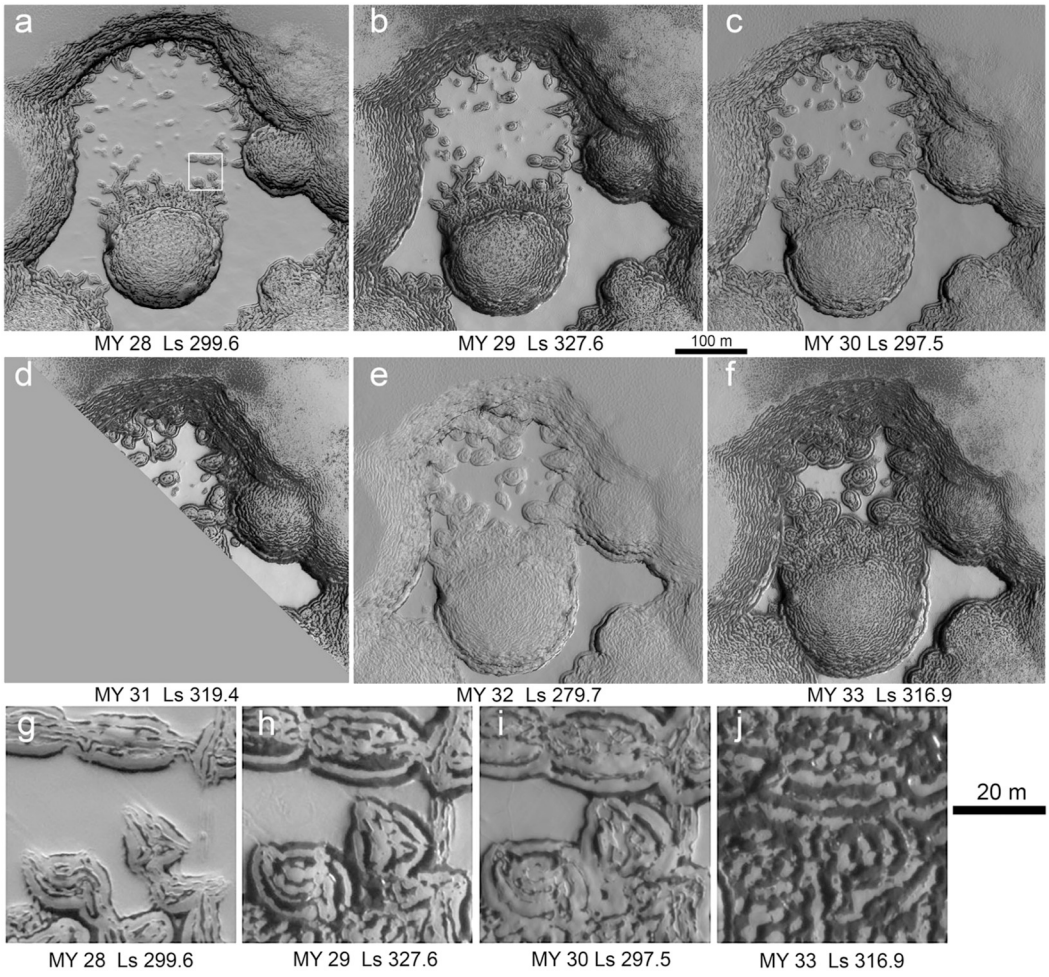

Fig. 8. Five Mars years of evolution of reticulated surface: (a)–(f) Centered at 86.3°S, 1.5°W. HiRISE Images are PSP_005006_0865_RED, ESP_014444_0935_RED, ESP_022593_0935_RED, ESP_31889_0935_RED, ESP_39854_0935_RED, and ESP_49467_0935_RED. (g–j) Detail of pit evolution into reticulated terrain. Multiple orientations of lineations are especially clear in Fig. 8g. (g)–(j) Expanded detail; location shown by box in (a).

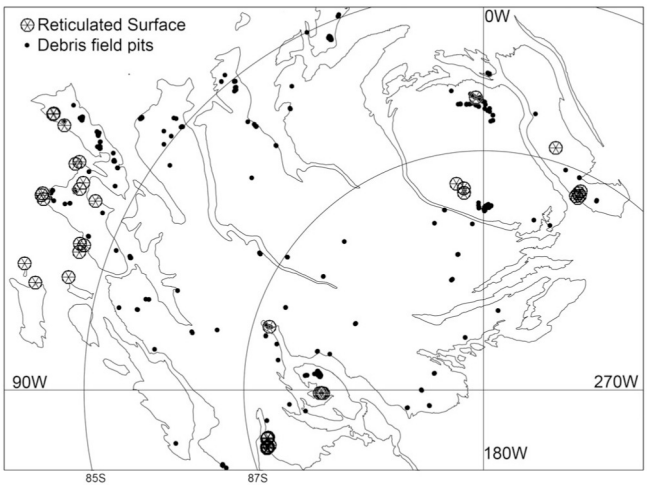

Fig. 9. Occurrences of reticulated surface morphology and debris field pits. Points for individual pits overlap; data for 690 pits are plotted.

- Debris ramp widths of 40–80 m in the thick A0 materials suggest lifetimes of 10–20 Mars years.
- Concave profiles of debris ramps suggest effective downwasting rates decrease rapidly after scarp passage.
- Wide accumulations of debris, "debris fields," up to several hundred m across, commonly mimic the plan shapes of mesas in A0 materials. They occur in most parts of the RSPC.
- Debris fields have been observed to survive as much as 24 Mars years.
- Debris fields originate by formation and merging of pits in the surface of a mesa rather than by retreat of a perimeter scarp.

Below we explore some of the consequences of aging debris fields, in particular, we examine relief inversion.

5. Contemporary evolution of debris fields: aging, final loss, and new accumulation

5.1. Introduction

In this section we examine behavior of debris fields associated with A0 materials, especially the old age and final loss of debris fields within the Tooth. This area has the best image coverage of debris fields, shows a progression of debris morphologies, and shows the development of new ice deposits after loss of the old debris. We document other regions of debris, including ramps, chiefly in the Supplemental materials to illustrate the commonality of different regions.

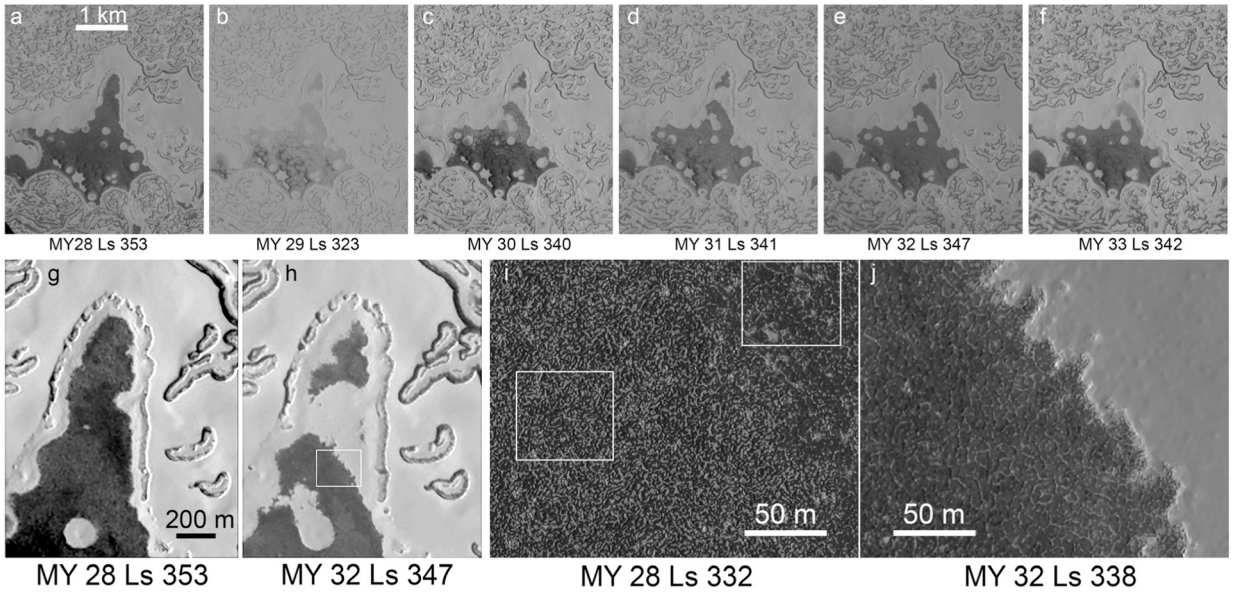

Fig. 10. Development of debris field at 86°S, 0°W, the "Tooth." See also Fig. 7. (a) MY 28 CTX image P13_006229_0951_XN_84S014W_071124. (b) B12_014338_0937_XI_86S000W_090817, (c) G14_023542_0937_XI_86S000W_110804, (d) D13_032456_0937_XI_86S000W_130629, (e) F14_041344_0937_XI_86S000W_150523, (f) J14_050060_0938_XI_86S001W_170401. (g-h) Development of additional area of residual ice in the Tooth. The new ice deposit forms in an area that was relatively slightly darker in MY28; see panels (g) and (i). Location of panels (i) and (j) are shown in the MY32 panel (h). (i) MY 28 view straddling boundary of new ice that formed in MY 29 and subsequently persisted. Image PSP_005728_0935_RED, Ls 332°. Rectangles show areas covered in Fig. 11: upper right box is for Fig. 11a; lower left box for Fig. 11b. (j) View of boundary in MY 32, image ESP_041146_0935_RED in MY32, Ls 338°.

5.2. New residual ice and contemporary inversion

Part "Ta" of the Tooth (Fig. 7c) is a senescent debris field. It lacks a pattern of nested pits and their associated topographic and albedo patterns, and has topographic and albedo patterns chiefly discernable only in MOC or HiRISE data. Shadows within it (Sec. 5.5 below) and comparisons to nearby B unit layers show its thickness above the substrate likely under 1 m. As such it may provide an end-member view of processes in the gradual loss of debris field materials.

The "Ta" region of the Tooth remained dark from MY 9 to MY 28 (Observed in MY 9, MY 12, MY 24–28; see Figs. 14 and 15 in T2009) while the debris field to the south (areas Tb, Tc, Fig. 7c) evidently emerged from an A0 mesa that was visible in MY 9 (Fig.7a, b), of which a small remnant survives. The "Ta" region was uniformly dark in the first high resolution images in MY 26 (Fig. S13). On a more recent time scale Fig. 10 shows that the "Ta" part of the Tooth has gained partial bright coverings since MY 29, twenty ♂y after it was first observed. What attracted particular attention to this marking was the observation that the major area of new bright material coincides with a subtly darker region of the Tooth in MY 28 (Fig. 10g, h). This reversal of contrast suggested the presence of local properties that might shed light on some controls of net gain or loss of CO_2 ice.

Fig. 10 examines the development of the new ice in the Tooth at progressively higher resolution. Fig. 10i and j show late summer views in MY 28 and MY 32 that straddle the boundary of the area developing new residual ice after MY 28. In MY 28 the brighter area had a more vermiform pattern, while the darker area, which soon accumulated new ice, had a more polygonal pattern similar to exposures of PLD materials. Fig. 11 zooms in and examines eight time steps in the six Mars years of the two marked areas in Fig. 10i. The area accumulating ice (Fig. 11 "a" panels, and area R1_8, Sec. 6) after MY 28 starts with prominent polygonal topography typical of PLD surfaces. In MY 29 and subsequent years, this topography is progressively muted by increasingly thick CO_2 ice covering. The "b" panels of Fig. 11 show the vermiform topography of the debris that does not accumulate residual ice until possibly MY 33 (area R1_9, Sec 6); that vermiform pattern is visible through early MY 32, but largely vanishes late in MY 32. HiRISE views in MY 33 only extend to Ls 317°, but CTX coverage at Ls 342° in MY 33 suggests the presence of new CO_2 ice. Additionally, recent CTX data in MY 34 indicate that the area in Fig. 11b panels is covered with ice through Ls 342° (Fig. S14). This area did not have new residual ice covering at Ls 342° in previous years, as dealt with quantitatively in Section 6 below. Both parts of Fig. 10i and j have transitioned from debris field to a PLD or PLD-like surface then to accumulating ice.

This sequence of debris transitioning to PLD surface to accumulating ice, combined with the generally uniform appearance of part "Ta" of the Tooth through MY 28 (Fig. 7) suggests that this portion of the Tooth has been covered by debris the entire viewing period and only recently has uncovered a PLD surface that retains seasonal ice.

The Fig. 11 "b" panels through MY 32 reveal repeated year-to-year reversals of contrast and inversions of topography: small bright positive features in later views become dark depressions, and vice-versa. The common presence of fine-scale relief inversions in the debris was surprising, even though fossil relief inversion in the RSPC at much larger scales had already been documented (T2005; T2016). Inverted relief is topography that has undergone reversal of relative heights (Pain and Ollier, 1995; Williams et al., 2009). Typical terrestrial examples involve erosion of a lava-filled fluvial channel, where the lava is more resistant to erosion than is the material enclosing the channel. Cementation of fluvial sediments can result in the same effect. Inversion of fluvial channels on Mars has been well documented (e.g., Morgan et al., 2014). As fossil relief inversion in the RSPC has been dealt with in some detail (T2005; T2016) we have put its discussion and updated maps in Supplementary Section 2.

5.3. True longevity: survival of debris

We examine the small-scale behavior of the portion of the Tooth that has remained relatively dark in summers throughout MY 26 (Fig. S13) and MY 28–34 (Fig. 12). Fig. 12a shows a complex, changing mix of irregular, vermiform, spotty bright and dark areas including patterns that repeatedly reverse contrast year-to-year. These are not the one-time

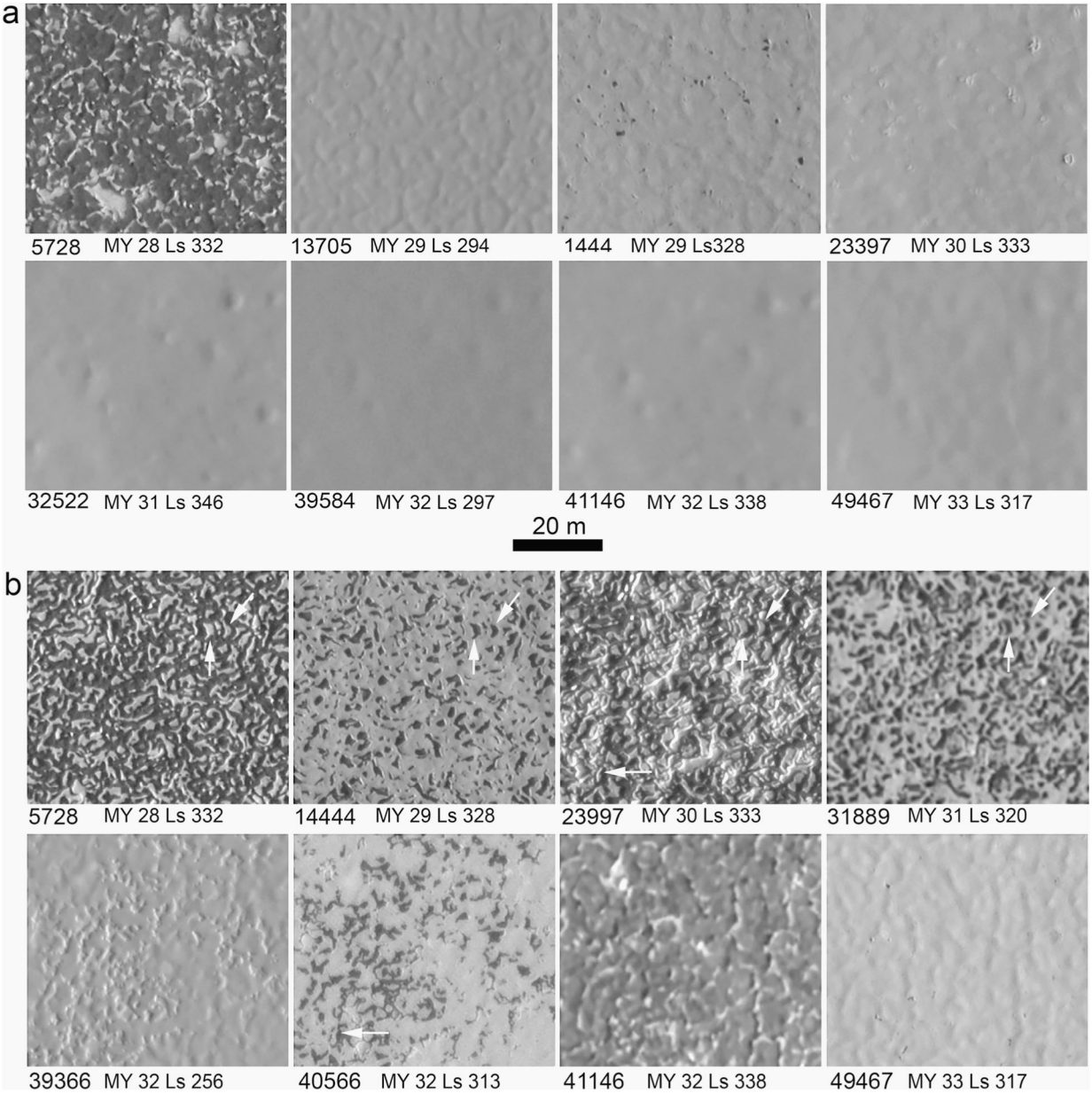

Fig. 11. Development of new ice cover after MY 28. Locations are shown in Fig. 10i. (a) Area within area R1_8 (Sec. 6 and Fig. 19) that shows transition from PLD surface to new ice accumulation. Frame labels are MRO orbit number, Mars year, and Ls. Frames are individually stretched to show surface textures. Centered at 86.30°S, 0.50°W. (b) Area R1_9 (Sec. 6 and Fig. 19) that shows progression from thin debris cover to PLD surface to new ice accumulation. A common pair of features in top row is shown by white arrows. Horizontal arrows in panels for orbits 23,997 and 40,566 relate features in rapidly changing appearances. Vermiform texture is retained through MY 32 Ls 313°, but a polygonal surface, apparently PLD material, shows at the end of summer in MY 32 Ls 338°. Centered at 86.30°S, 0.52°W. The MY 33 panel, at Ls 317° suggests new ice thinly coats a surface with the polygonal topography of PLD materials. MY 34 images confirm new ice has covered this region; see Fig. S14.

reversals of fossil relief inversions (Supplementary materials and T2005), but a back-and-forth of contrasts and topography over five Mars years. The relative topography is evident in spring images (Fig. 12b) where albedo contrasts are covered by the seasonal ice and the solar elevation is low. These spring images confirm that the bright = high, dark = low pattern of the preceding late summer lasted until accumulation of stabilizing winter ice. The high-contrast, late summer images of Fig. 12a are difficult for shadow analysis, but the brighter areas are shown to be higher by a few clear shadows.

The sequence of changes leading to inversion of relief in a single spring/summer are illustrated in Fig. 12c. Viewing the changes in the top row (a slight extension of the area in Fig. 12a and b) is best started by focusing on the diamond-shaped positive relief feature also prominent in panels a and b. At Ls 285° this diamond form is one of many positive features (illumination is from the left) with flat areas in between. By Ls 299° many of these positive relief features have developed small trenches around much of their perimeters, some of which have already consumed the smaller, previously high-standing material. At Ls 303° these trenches have expanded and have removed much of what had been positive relief. By Ls 317°, shown in Fig. 12a, the great majority of what had been positive forms at Ls 285° are now negative relief. Much the same sequence appears in the MY 29 images at the bottom of Fig. 12c. Here at Ls 294° marginal troughs have started to form around some of the positive relief forms; by Ls 304° many of these have merged into pits

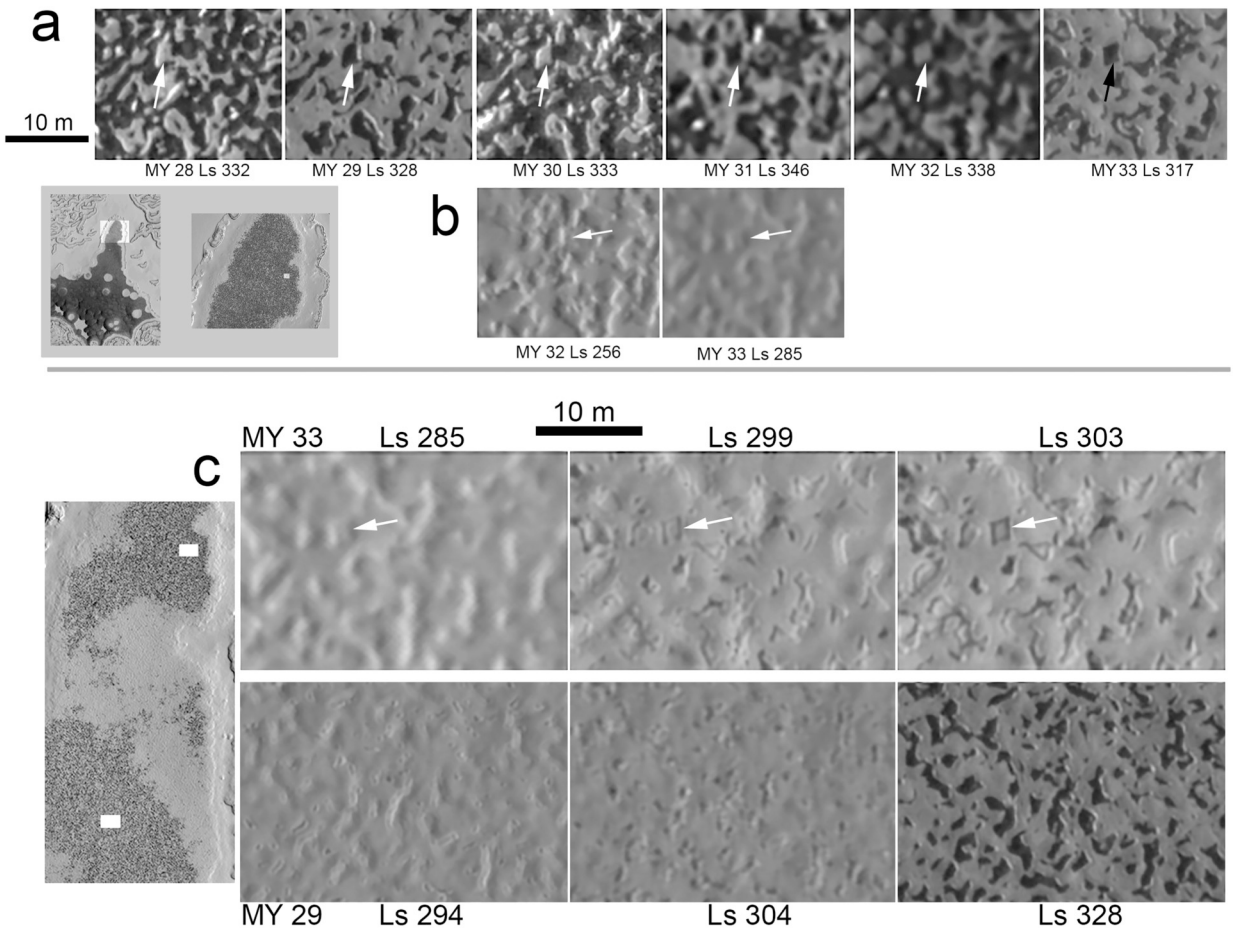

Fig. 12. Seasonal activity in senescent debris in the "Tooth." Sun is from left in all frames (some variation of azimuth). (a) Late summer HiRISE images, left to right, PSP_05728_0935_RED; ESP_14444_0935_RED; ESP_23397_0935_RED; ESP_32522_0935_RED; ESP_41146_0935_RED; ESP_49467_ 0935_RED. Centered at 86.29°S, 0.48°W. Arrows show common diamond-shaped feature that is positive relief in MY 28, 30, and 32, and negative relief in MY 29, 31, and 33. (b) Spring images with seasonal CO_2 ice coverage showing the relative topography. White arrows note the diamond-shaped feature from row "a;" it is negative in MY 32, and it is positive again in MY 33. (c) Early summer development of relief inversion in two locales in MY 29 and 33. Location key from ESP_14444_0935_RED, MY 29; compare to Fig. 10g. Location key upper box is for upper row of panels; lower box locates lower row of panels. Upper row is part of region R1_10. Lower row part of region R1_9.

that commonly mimic the outlines of their predecessor positive relief forms. By Ls 328° inversions are widespread and the floors of the pits are relatively dark. Similar examples of repeated reversal of brightness and relief at horizontal scales of 1–3 m have been found in floors of the heart-shaped pits in unit A1 (Fig. S15).

In Fig. 12c the spring images show a flat, lower surface; late summer images (Fig. 12a) show a flat upper surface. We cannot definitively relate the elevation of these surfaces and thus cannot firmly determine the amount, if any, of net lowering. The flat surface in these images is not the PLD surface that was exposed in MY 32 in area R1_9, Fig. 11b.

5.4. Contemporary inversion in a young, thick debris field

An archetypical example of debris field is shown in Fig. 1d; portions of it were almost certainly part of an A0 mesa in MY 9 (Fig. 7). Areas "Tb" and "Tc" of the Tooth (Fig. 7c) roughly coincide with the former mesa in MY 9, and possibly in MY 12. Area "Tc" is thus younger than area "Ta." All of area "Tb" may not have been an A0 mesa in MY 9, but its greater thickness than "Ta", preservation of nested pits, and its albedo (Sec. 6 below), and gradational relation to Ta and Tc indicate that it is intermediate in age to areas "Ta" and "Tc" (T2009).

Fig. 13a shows the spatial transition (in MY 28) from youngest, thickest debris in the Tooth to the thin, senescent debris in the tapered, northern part. Characteristics of debris in this area include: 1) The nested, bowl-profiled depressions separated by rounded crests and marked by bright and dark markings trending roughly parallel to the crests. 2) The transition, lower left to upper right, from "Tc" to "Tb" and to "Ta". The "Tb" to "Ta" transition is close to the location of the margin of the bright form (presumably A0 mesa) recorded in MY 9 images by Mariner 9 (Fig. 7). 3) ~180-m diameter flat-floored depressions within the debris that currently expose PLD partially coated by bright ice. These depressions gained more bright ice covering after MY 26 (Figs.7, 13, S13). The affinity of the polygonally-cracked PLD surfaces in these depressions for new deposition appears to be the same as that developed in MY 29 to 32 in the "a" part of the Tooth (Sec. 5.2).

5.5. Geometry of relief inversion in debris fields

The amplitude of the topography subject to reversal can be estimated from shadow lengths, although these are limited in number because of viewing constraints, and because of the limited flat space in which shadows can be cast and be unambiguously measured. Nevertheless, the measured relief in the regions shown in Figs. 11 and 12 is between 0.2 and 0.4 m (Table S4). There is a caveat to these height estimates in the spring: the contribution of possibly transparent seasonal ice. However, these samples have small impact on average heights (Table S4). The lack of clear fiducial marks for height or depth limits our ability to estimate net downwasting rates (if any). In many areas, such as that shown in

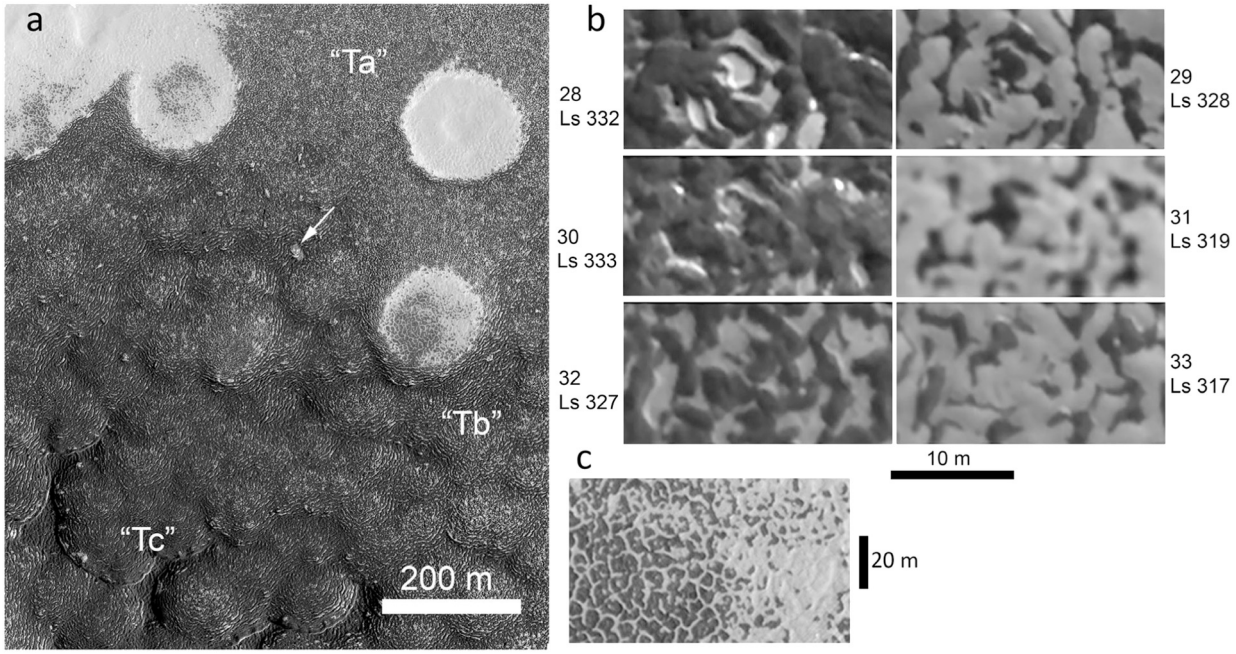

Fig. 13. Relief inversions and polygonal surface of underlying PLD in region "Tb" of Tooth debris. (a) Context of transition from youngest section, "Tc," at lower left to "Ta," oldest, in upper right. Compare to Fig. 7. Image PSP_05728_0935_RED. MY 28, Ls 332°. (b) Summer appearance of area in upper center of "Tb," Identified in panel (a) by arrow. Panels identified by MY and Ls. Some forms reverse year-to-year; patterns become altered after >2 Mars years. Full image list is included in Table S5. (c) Exposure of underlying PLD materials with polygonal troughs. This polygonal surface is one that develops new ice cover after MY 28 (Figs. S13, S14).

Fig. 12, no reference level can be inferred confidently. However, in Fig. 11, there are hints of polygonal terrain emerging as early as MY 31.

5.6. Seasonal behavior milestones in debris fields

Common seasonal milestones in debris areas near 86°S, 0°W and 86.8°S, 344°W are summarized in Fig. 14. Small dark fans are the first sublimation-related features to appear in debris ramps, generally in the Ls range of 220–250°, but as late as Ls 270°. Fans are far more prominent in debris ramps that have long, narrow, parallel ridge and trough topography than they are in the more equidimensional relief of debris fields. Fans also occur in some of edges of B unit materials in the Tooth region, and elsewhere in the RSPC (Buhler et al., 2017). Dark areas form on crests and bases of ridges in the Ls 250–300° range (Fig. 14) in both the debris fields and debris ramps. Within the debris fields, troughs forming along the sides of positive relief features and indentations in the ridge crests at these times constitute the initiation of relief inversion (Fig.12c).

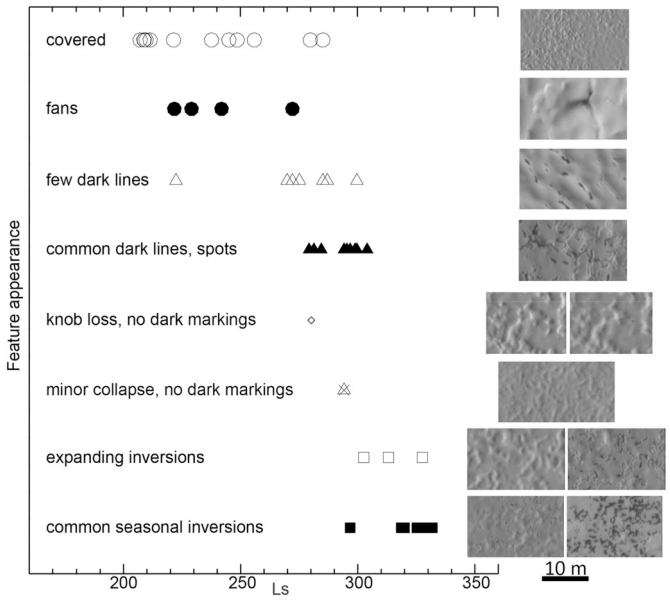

Fig. 14. Milestones of spring and summer changes in debris fields and ramps. HiRISE image fragments illustrate milestones tabulated in Table S5. Ls is that of first detection of a change; "covered" is the last view without obvious change from previous coverage. Horizontal spacing of the dates indicates the general frequency of observation.

More extensive development of inversions of ridges and small mesas occurs in Ls 280–310° (Figs. 12, 14, and S16). Small (<2 m across) knobs disappear without visible darkening just before dark spots and ridge lines appear in MY 32 in the R1 area (Fig. S17). The data shown in Fig. 14 are listed in Table S5. These milestones in the spring and summer activity on the RSPC are examined further in Section 6 covering photometry.

5.7. Possible early evolution of the Tooth

The relationship of part "Ta" of the tooth to the scallop-shaped mesas of A0 materials that are the common nurseries for debris fields is not obvious. Instead, part "Ta" of the Tooth resembles nearby tapered, dark windows in the B unit (Fig. 7d, e). Such tapered dark regions, usually found within B unit materials originate at mesas of both B and A unit materials (that is, mesas ~3–10 m in height (T2005, Fig. 22). These markings bear a strong resemblance to wind streaks observed at lower latitudes. The wind streaks are interpreted to form from both erosion and deposition in the lee of topographic obstacles due to enhanced erosion or to wind shadowing, depending on atmospheric stability (Veverka et al., 1981; Thomas et al., 1984; Lee, 1984; Iversen and Greeley, 1984Greeley and Iverson, 1985). Over 700 dark, tapered markings have been mapped on the RSPC for other work in progress. In this paper we refer to these areas as "wind-cleared" regions on the basis of their close resemblance to obstacle-related wind streaks observed at lower latitudes that involve erosion and deposition of dust and sand. The

possibility that the shape of the Tooth may have been initially influenced by wind activity is discussed below in Sec. 7.

5.8. Summary of debris field inversions

- Debris fields and debris ramps show year-to-year inversions of small scale (<5 m across, <1 m high) relief. Relatively bright, relatively high forms visible in late summer are replaced the following summer with similarly shaped, relatively low, relatively dark forms. Some of these shapes repeat for as many as three Mars-year pairs; others change their outlines over time.
- These local relief inversions begin in early spring with the appearance of darkening centers and marginal troughs on local positive relief forms at about Ls 285–290°. By Ls 310° many of these formerly positive relief forms are darker, negative relief forms. Springtime images that lack complications of albedo confirm the year-to-year topographic inversions.
- Some relatively bright ice remains visible in patchy and vermiform patterns in the debris until the latest summer observations.
- Final loss of debris from underlying PLD materials appears to facilitate (but not require) renewed accumulation of new residual CO_2 ice.

6. Photometric aspects of debris fields and associated changes

We conduct a simple photometric analysis to aid in discriminating different materials and changes in the RSPC and to test the role photometric properties may play in the seasonal and long term behavior of the RSPC's CO_2 ice cover. We use CTX images calibrated to give Lambert albedos using software provided through Malin Space Science Systems ("makemap"). These data are broad-band, largely sensitive to radiation between 500 and 700 nm (Malin et al., 2007). HiRISE data are also used as supplied from the HiRISE site (https://www.uahirise.org/anazitisi.php); these are mostly RED images, sensitive between 570 nm and 830 nm (McEwen et al., 2007). No atmospheric corrections are applied. The surface of the RSPC is expected to have varied photometric functions, with consequent varied relationships to the calculated Lambert albedos. Most comparisons made here involve low emission angles, have incidence angles varying between 66° and 87°, and use portions of the same image with essentially the same viewing geometry and atmospheric properties. Atmospheric properties vary largely due to dust loading which is obvious in some of the data.

Our CTX photometric data are primarily from five sites that are shown in a key in Fig. 15. The complete set of seasonal and averaged plots are given in Figs. S19 – S28. Averaged albedos at the different milestones are given in Table S6.

6.1. Year-to-year reversals in the Tooth from HiRISE data

The year-to-year reversal of much of the brightness patterns shown in Fig. 12a invites quantitative description of the back-and-forth albedo

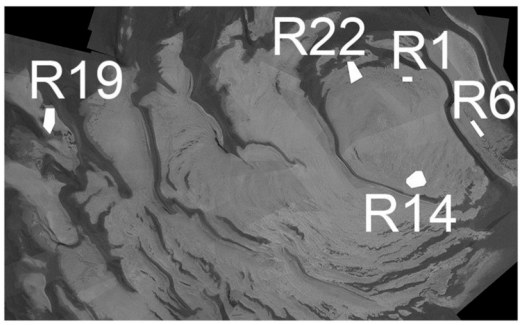

Fig. 15. Photometric sampling regions.

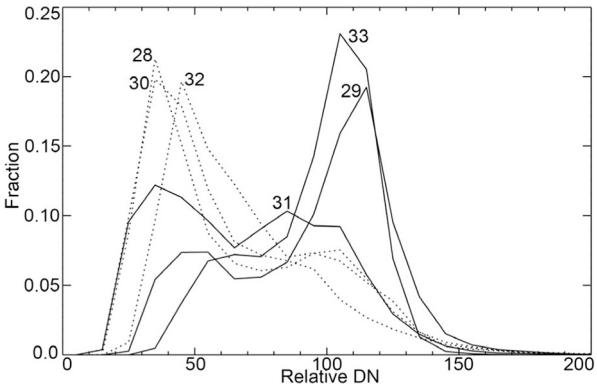

Fig. 16. Year-to-year reversals of brightness distribution in part of the "Tooth." Histogram of relative brightnesses in areas (190 × 147 pixels) centered on frames of Fig. 12a. Curves are labelled by Mars year.

changes. Histograms of radiance values for each pixel in Fig. 12a frames expanded to 190 by 147 pixels at 0.25 m/pixel are shown in Fig. 16. The radiances are scaled such that each image's histogram reaches the same top brightness bin. With the exception of MY 31, odd numbered Mars years are skewed to brighter values, even numbered Mars years are skewed to darker ones. For these six observation times, the brighter materials average an albedo ~1.4 times that of the area average, the darker areas average ~ 0.70 times the area average. Thus the darker, unresolved component of CTX data for the debris field could be ~30% below the average albedo, keeping in mind that these are values for the "RED" HiRISE images. This possibility is important in evaluating CTX data for the different summer darker areas of debris fields and possible PLD exposures in wind-cleared areas.

6.2. Debris fields compared to dark wind-cleared areas

We compare the two most common dark features in the RSPC: debris fields and wind-cleared exposures of (likely) PLD materials, examining the seasonal and year-to-year photometry. Fig. 17 shows three aspects of the data covering one wind-cleared region (R1_3; Fig. 17 key) and two nearby debris fields. One debris field is in the "Tooth" (R1_5; within the area Fig. 13a), and one (R1_6) is adjacent to a mesa remnant of A0 material. The top row of plots in Fig. 17 shows the individual measurements of Lambert albedos of the sample areas. The middle row shows ratios of those measurements to those in an area of unit B (R1_1), a flat, ostensibly uniform surface and the brightest surface in the region. The bottom row of Fig. 17 shows the averages of the Lambert albedos in 10° bins of Ls. Effects of atmospheric dust are evident, most notably in the MY28 data between Ls 250° and 300°, and probably in the wide ranges of values in different years between Ls 300° and 350°.

The top and bottom panels of Fig. 17 show seasonal patterns that are broadly similar in other areas on the residual cap. The steady, reproducible rise in calculated albedo from Ls ~190° to Ls 250° is followed by a flattening, or even slight decrease of the calculated albedo. The albedo then decreases rapidly from local maxima at ~Ls 295°–305° to minima reached at Ls ~330°–350°. Data taken in late summer (usually after Ls 355°) sometimes show increases in calculated albedos. These increases may result from onset of new deposition (James et al., 2009), effects of increased atmospheric contribution, or a more pronounced failure of the assumed photometric function of the surface at extreme incidence angles.

The wind-cleared area, R1_3, relatively dark since MY 9, is safely interpreted as an exposure of PLD materials from the polygonal patterns visible in high-resolution images (Figs. 8, 13d, and S8). Fig. 18 shows ratios of the albedos of this wind-cleared PLD to those of two debris field sites. In the broadband CTX data the PLD exposure R1_3 is usually 10–15% darker in the summer than the debris fields.

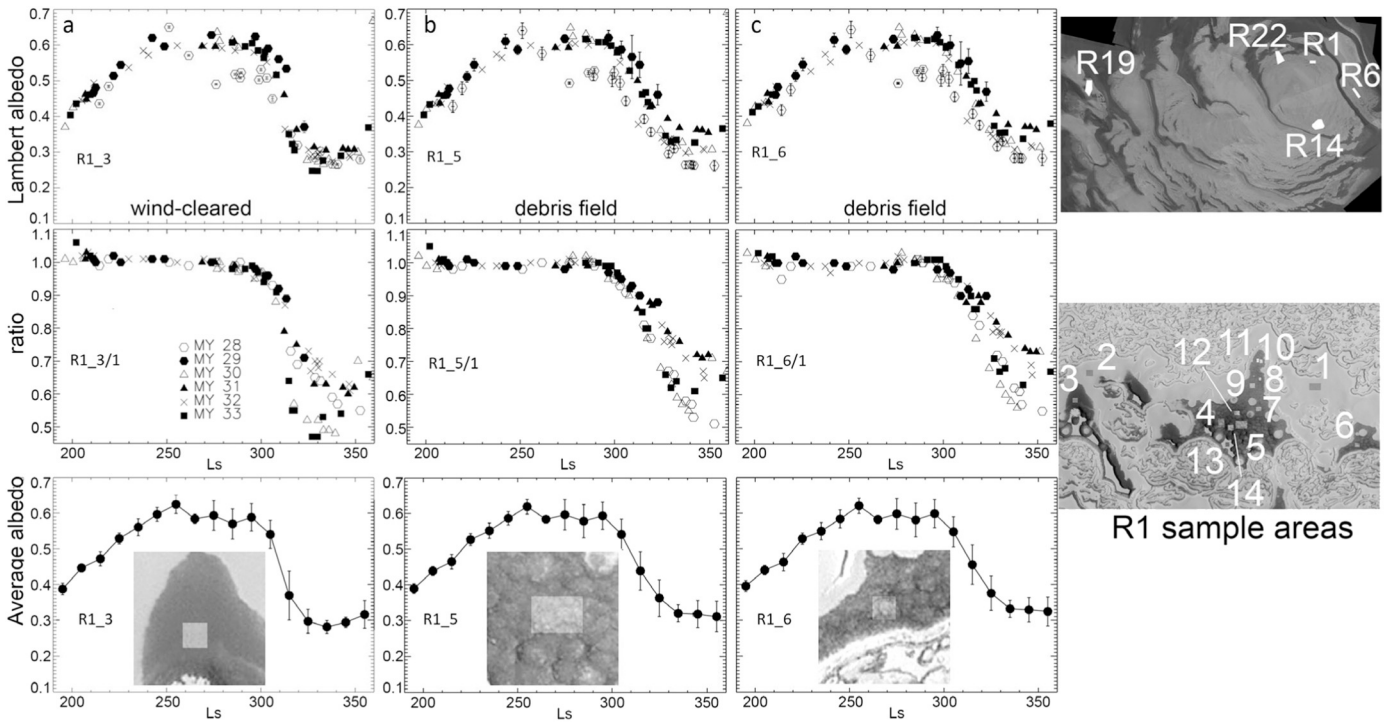

Fig. 17. Photometry of debris fields. (a) R1_3, is a dark, wind-cleared region, likely an exposure of PLD materials. (b) Area R1_5 is within the main debris field, in the lower part of Fig. 13a. (c) Area R1_6 is in a separate, nearby debris field. Key for all regions sampled in the RSPC and areas within Region 1 are given at right. Top row of plots contains all individual measurements of sampled areas. Sample sizes, generally 100–330 m across, are dictated by space minimally interrupted by pits or other topography not typical of the unit. Error bars are one standard deviation of values within the sample areas, and are shown only for Mars years 28 and 29 to reduce visual confusion. Most error bars are smaller than the data symbols. Second row displays ratios of these areas to a flat section of B unit material. Bottom row shows averages, in 10° Ls bins, of the data in the top row; error bars are one standard deviation. Local context and sampling areas shown in bottom row.

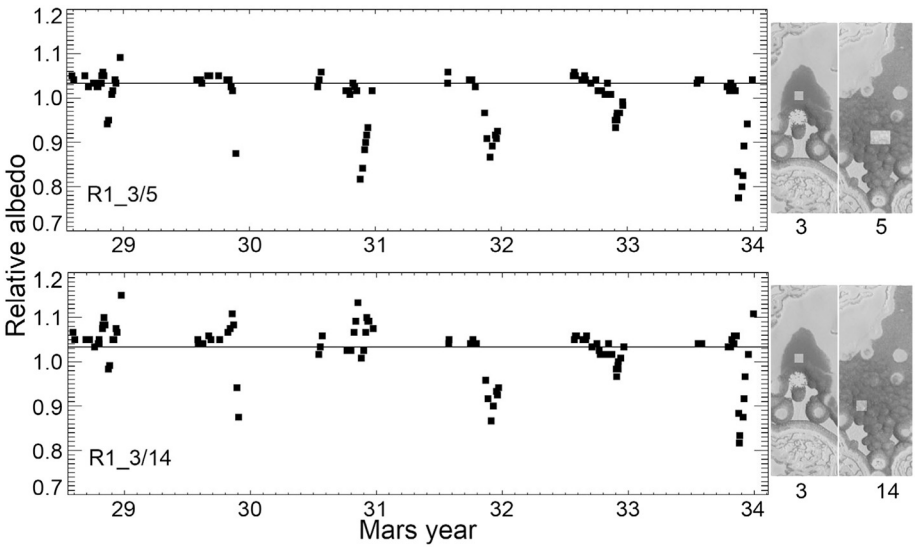

Fig. 18. Relative secular behavior of the wind-cleared region R1_3 and debris field samples (R1_5 and R1_14) in the main Tooth feature, area "Tc.".

We expand the wind-cleared comparison to the debris in Sec. 6.5 after examining the seasonal milestones of the debris fields in Sec. 6.4.

6.3. *Differences within debris fields*

Fig. 19 shows secular behavior of the area of the Tooth's senescent debris field examined in Sec. 5 and Figs. 11 and 12: region R1_8 is within the area that became ice-covered after MY 28 (Fig. 11a), region R1_9 remained a typical, relatively dark debris field through MY 32 (Fig. 11b). Fig. 19, column a, top, shows the data for region R1_8; its ratio to the area R1_1 data is shown at the bottom, and illustrates the difference in MY 28 from all subsequent years as ice builds up in this region to become morphologically noticeable. The ratio of R1_9 to R1_8 shows the reversal of contrast after MY 28. The continuous record, the second panel of column c in Fig. 19, shows a consistent, repetitious seasonal pattern. Area R1_9 in MY 33 is decidedly brighter than in

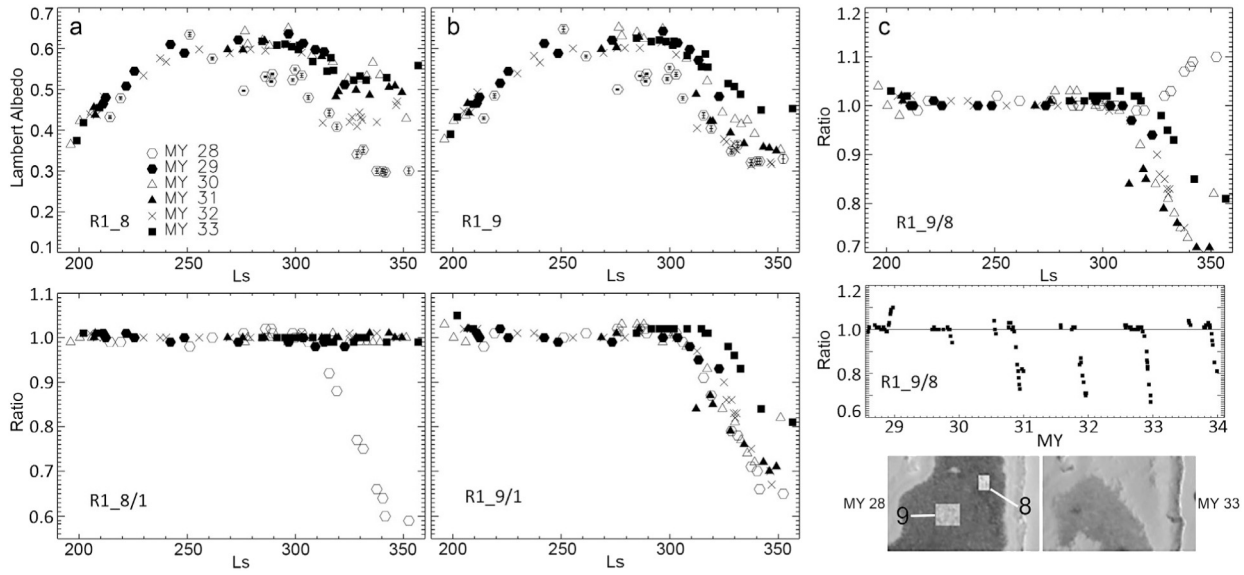

Fig. 19. Seasonal and secular behavior of the "Tooth." (a) Area R1_8; (b) Area R1_9. Top columns of (a) and (b) show individual data points. R1_8 accumulated ice after MY 28, and R1_9 maintained its albedo during the observations of MY 28–33. (c) Ratio of area R1_9 data to area R1_8. Top panel shows seasonal ratios; middle panel shows secular behavior over the continuous period MY 28 to MY 33. MY 29 data were interrupted by a period of spacecraft safe mode, and we cannot differentiate late summer MY 29 activity from that in succeeding years.

previous years. As of this writing, MY 34 photometric data have not been processed, but as noted above in Sec. 5 and Fig. S14, area R1_9 retains bright material late into the summer, suggesting that the trend in the bottom plot of Fig. 19c will remain close to a ratio of unity in MY 34.

Area R1_8 suddenly started preserving winter ice in MY 29, after apparently remaining "dark" since MY 9. Area R1_9 is now dominated by the polygonal patterns indicative of PLD surfaces, and apparently is starting to preserve residual ice (Figs. 1, S14). Area R1_11 (see key in Fig. 17; R1_11 is west (left) of area shown in Fig. 12c, top row) began changing relative to area R1_10 in MY 31, but the relative albedos have neither monotonically changed nor become stable (Fig. S31). The behaviors of areas R1_8, R1_9, and R1_11 show affinity for new net deposition in areas that expose the PLD.

Other debris fields of interest are documented in the Supplementary materials.

6.4. Photometric milestones

We use simple averaging to test the consistency of our sample areas' seasonal behavior. For Fig. 20 we have taken average data, such as those in Figs. 17 and Figs. S20, S22, S24, S26, and S28 and noted the time of summer inflection toward lower albedos, the time of late summer minima in albedo, and the time and value of maximum calculated albedo. The latter is sometimes coincident with the inflection value, but sometimes it occurs closer to Ls 250°. We show the minimum albedo as a function of season, and minimum albedo as a function of the maximum albedo and as a function of inflection albedo.

The milestones of small-scale changes are compared to the average seasonal albedo behaviors of debris fields in Fig. 21. Fans (Fig. 14) are spring's first visible changes and occur during the period of consistent increase of calculated albedos for essentially every unit sampled. Given the small area of fans, their effect on albedos of sampling regions is small. The initial exposures of darker materials in collapse and inversions correlates with the period of relatively stable calculated albedo. This period of stable albedo also occurs in the reference B unit materials (R1_1, R1_2, R14_1, R14_2, R14_3, R19_1; Supplemental materials). It is not until Ls 290–300° when fractionally significant exposures of darker materials appear that these A unit materials noticeably darken compared to the B units samples that presumably represent the cleanest CO_2 ice. Yet the B unit samples also start a noticeable reduction in calculated albedo in the Ls 290–300° range (see plots in the Supplementary material). These common trends suggest there are common photometric functions effective on all the exposed surfaces for much of the illuminated seasons. The overall spring albedo trends have been attributed to effects of changing grain size and dust redistribution (Paige and Ingersoll, 1985; Kieffer et al., 2000; Langevin et al., 2007).

6.5. Comparison of wind-cleared areas and darkest component of debris fields

The results in Fig. 20 suggest that the wind-cleared areas (filled triangles) are darker on average in the CTX data than are the debris fields (solid dots). The sampled debris fields have a wide range of calculated albedos, an unsurprising result given the generally rough topography and variable amounts of included brighter ice throughout summer observations. Averages of the lowest calculated CTX albedos for debris fields from 14 locations in the six Mars years (Table S6) are 0.37 ± 0.07; the lowest albedos of wind-cleared areas average 0.27 ± 04. The debris field values are combinations of bright ice and a darker component (Fig. 16). The spatial scale of these albedo variations is only a few m (Figs. 11, 12), and thus the variegations are largely hidden when sampling 6 m-pixels in CTX data. Fig. 16 indicates that the dark material in area R1_10, has a calculated albedo (in the HiRISE RED images) ~ 70% that of the average albedo. If this proportion were applicable to CTX data for the dark area averages, it would imply that the dark component of debris fields, as observed by CTX, has calculated albedos essentially the same as those of wind-cleared areas: 0.26 compared to 0.27 for the wind-cleared PLD. Possible systematic errors, not least the comparison over different wavelength ranges, require great caution in use of these averages.

Trying to avoid the problems of comparing data with different wavelength sampling, we sample some HiRise data including both materials, for which there are some suitable HiRISE images. We compared wind-cleared and debris areas in three HiRISE images in late summer. These images included exposures of debris that were relatively smooth, and were oriented such that incidence angles for the nearby level areas of the PLD surface are similar to those on the debris field sample. In image ESP_14444_ 0935 we find an average albedo ratio for wind-

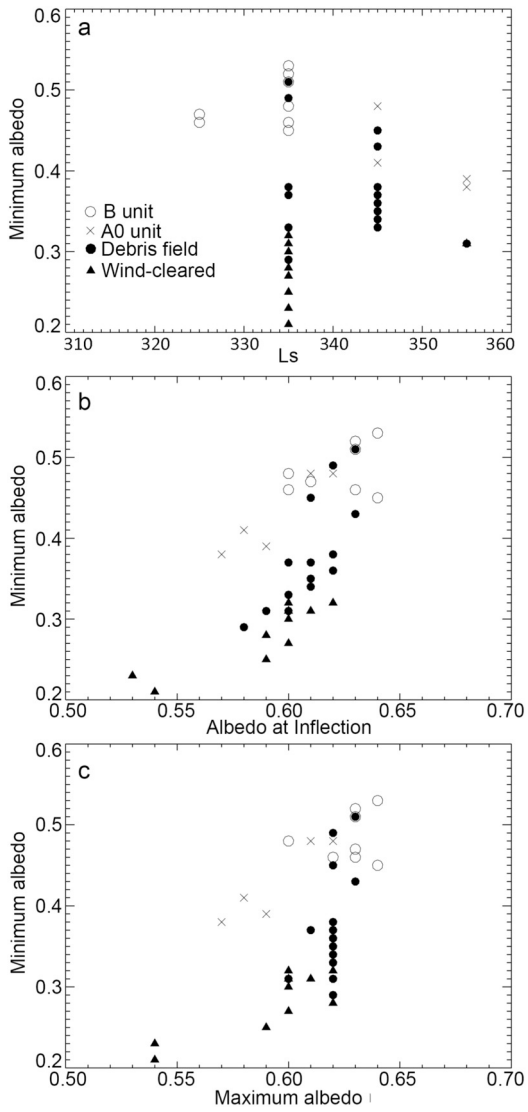

Fig. 20. Summary of CTX seasonal photometric results. (a) Minimum albedo and its Ls. See Table S6. Each symbol is the result from a particular sample site, such as R1_4. (b) Minimum calculated albedo versus the calculated albedo at inflection. (c) Minimum calculated albedo versus maximum average calculated albedo. The general character of individual point uncertainties can be seen in individual plots in Figs. S19, S21, S23, S25, and S27. Error bars for the average data are shown in Figs. S20, S22, S24, S26, and S28.

cleared to debris field (WC/DF) of 1.1. In PSP_005728_ 0935 WC/DF is 1.34, and in ESP_49768_0930 WC/DF = 1.11. These crude comparisons suggest that some small differences between the surfaces might be demonstrated in a more detailed study, but here we cannot claim a real differentiation of the surfaces based on these calculated albedos.

6.6. Summary of photometric results

- Calculated albedos of debris fields result from a spatial mix of darker material and brighter recent ice deposits (Here "ice" is likely to be CO_2; water ice contributions are apparently small (T2009)). HiRISE data suggest the brighter ice has a calculated albedo ~1.4 that of the local area average and that the darker component is ~0.7 times the local area average late in southern summer.
- Exposed PLD or PLD-like surfaces within the RSPC cannot in general be distinguished from the dark component of debris fields by the broadband visible albedo. However, there are suggestions from HiRISE data that some of the wind-cleared areas (exposures of PLD) have slightly higher calculated albedos than the dark component of debris fields.

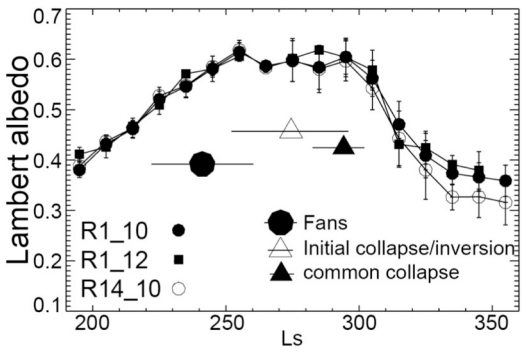

Fig. 21. Milestones and average seasonal photometry. Average seasonal CTX calculated albedos for three debris fields are shown with average Ls for appearance of fans, early collapse, and widespread collapse seen in HiRISE data. Horizontal error bars are one standard deviation. All average curves are in Figs. S20, S22, S24, S26, S28.

- Nearly all the calculated CTX albedos of debris fields in spring rise consistently until Ls 250°. Between Ls 250° and 290°–310° calculated albedos are nearly constant, followed by rapid declines until Ls 330–350°. Some regions show slight rises in calculated albedo after Ls 330°, which are likely affected by atmospheric scattering and inadequacies of applied photometric function for the surface; some brightening might result from early seasonal deposition of ice (James et al., 2009). Albedo minima for debris fields tend to occur slightly later than for wind-cleared areas and the B units.

Finally, what is the relatively dark material in the debris and in the PLD or PLD-like exposures? Initial results presented by T2009 showed that water ice was a small component of debris ramps surrounding mesas and the upper surface of the PLD. Modeling of coarse resolution data from OMEGA estimates that water ice is at most 0.02 to 0.06 wt% of the residual ice surface (Douté et al., 2007). More recently, water ice is noted to be a spatially variable component of debris fields (Calvin and Seelos, 2017) along with variable path lengths in CO_2 ice, and variable amounts of non-ice material. Detailed modeling of high-resolution CRISM data is underway. Freshly collapsed A unit materials are relatively dark (Figs. 8, S5, S9) as is some debris from B unit materials (Fig. S4a-c), although much of the dark material showing in B unit margins could be the underlying PLD (Fig. S12c). Many of these exposures in A and some B unit outcrops suggest a darker zone or layer below the surface. Because this darker zone appears to occur in a variety of units, but always is stratigraphically lower than surficial bright materials, the dark debris may simply be old (>1 ♂y) dirty ice. Exposures at the margins of the residual CO_2 bright surfaces (not the debris we are addressing here) can be water-ice rich, and include a large fraction of dust (Douté et al., 2007). Aging of either snow or glaze ice might involve fracturing or even redistribution of included dust. Dust redistribution (lofting or sinking) from absorption of insolation may be common in seasonal CO_2 ice deposition and may significantly affect its albedo (Kieffer, 2003; Kieffer et al., 2000; Hansen et al., 2010; Portyankina et al., 2010). The changes in Figs. 11-14 include new annual CO_2 ice, and there is no reason to exclude older ice from also being subject to alteration of dust distribution or grain sizes, or from retaining some of those effects that occur in seasonal heating.

7. Debris evolution: possible mechanics, and significance

Do the debris fields survive longer than observations of debris ramps would suggest? The asymptotic average ramp profile in Fig. 3 and the size distribution in Fig. 2a suggest that some parts of debris fields or ramps survive well beyond the average lifetime, that is, for several Mars

decades. The question becomes how does a slowing vertical change rate operate, or, how is a low horizontal loss rate of thin remnants enforced? The distinctive character of the eroding debris is its locally rough topography and its exposures of different albedo materials on scales of cm to a few m. The occurrence of bright ice late in the summer in the small-scale debris topography, and the cycles of relief inversion, suggest that trapping of new ice in low areas may contribute to a reduced average loss of materials. The form of new seasonal ice within the RSPC is not definitively established (Hayne et al., 2012, 2014) as proportions of snowfall and surface condensation may vary by time and locale.

7.1. Heating: geometric and albedo effects on loss and retention of ice

The spring loss of materials and changing albedo starts with fans and small troughs around knobs and other positive relief features, commonly followed by formation of troughs or other evidence of collapse at the crests of ridges or mounds (Fig. 14). These changes indicate that heating at depth is effective, something common in areas of seasonal ice (Kieffer et al., 2006; Piqueux and Christensen, 2008b; Portyankina et al., 2010; Buhler et al., 2017) and is suggested to be important in parts of the residual ice (Pathare et al., 2005; Line and Ingersoll, 2010). The early signs of loss are shown in Fig. 12c. The troughs along edges and crests of the positive relief features are ~1 m or less in width. The heating should be at a depth not substantially larger than the width of the troughs, perhaps 0.5 m. However, it is not immediately clear from experimental results (Chinnery et al., 2018, 2019) that seasonal insolation input at depths of >0.1 m under solid ice, or even less under snow, would be effective. Buhler et al. (2019) have modeled the surface deposition of CO_2 ice from subsurface heating of CO_2 beneath darker, warmer H_2O ice, but at much larger time and depth scales than the seasonal processes observed here. Until the larger scale polygonal patterns of the underlying materials are exposed (e.g., Fig. 10), the lower materials in all our observations of relief inversions appear to involve CO_2 deposits. Additionally, the only exhalation effects seen in our areas of interest involve darker materials, not bright CO_2 deposits. Thus, an analogy to the Buhler et al. model may not apply.

Heating at depth from insolation or conduction calls into question simple use of surface slopes for estimating loss rates from sublimation. However, the scale and location of this heating may help interpret events. The sequence in Fig. 12c is most simply interpreted as what stands high absorbs heat the most and suffers the most sublimation. Because of the high incidence angles, the depth of insolation absorption is mostly in the horizontal direction, that is, into the side of protuberances. Even at high incidence angles the wide flat areas should absorb insolation and lose material, but virtually all the darkening well into summer is in areas that were high standing. Buhler et al. (2017) note at 10 m scales in some B-unit materials sloping of mesa surfaces toward scarps may be due to preferred absorption on the steep slopes.

Although at small scales reversing topography seems not to follow simple expectations based on albedo, at wider scales the apparent loss rates correlate with average albedos. Within the Tooth, area "Tc" is youngest, thickest, and darkest (in late summer). Shadows show "Tc's" average surface is probably >6 m below the original mesa, and much of this loss appears, from shadows, to occur close to the mesa scarp. Within the "Tb" region the lack of shadows at incidence angles near 80° in its pits (that is, only subdued relief) and the small change in appearance during 6 Mars summers, indicates substantially thinner materials and slower downwasting rates than those in area "Tc." The "Ta" region has an even thinner cover (possibly all <1 m), is rough at horizontal scales of 1–3 m, and is the brightest of the three areas. We have measured late summer albedos (CTX data) for the entire areas of the three divisions in the Tooth (excluding part of "Ta" with new deposition in MY 29); the results are given in Fig. 22. The youngest, most rapidly changing one is darkest, while the oldest and most slowly changing area is brightest. The simple-minded conclusion would be that brighter areas are less subject to sublimation, or more subject to deposition. Yet much of the work

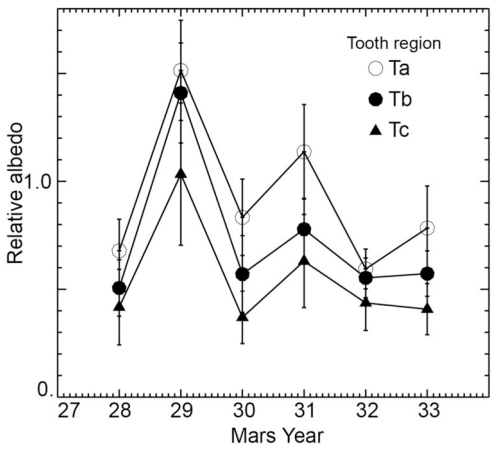

Fig. 22. Late summer albedos of Tooth regions using CTX data. See location key for areas Ta, Tb, Tc in Fig. 7c.

shown above shows that at horizontal scales <6 m, there are multiple components to the morphology, and they do not behave simply within or between seasons, though they do appear to behave in repeating patterns.

The relief inversions along fracture traces documented in Buhler et al. (2017) may involve some processes similar to some of those observed here, such as heating at depth, and collapse of surface materials, and effects of uneven topography on subsequent deposition. Those documented in Fig. 14 in Buhler et al. (2017) are on the upper surfaces of layered materials unlike the debris field examples studied here, and they do not appear to show long sequences of year-to-year reversals, as found here.

7.2. Some longevity factors

A possible difference between the evolution of ramps and debris fields might arise from the role of fracturing, slumping, block rotation, and further mechanical fragmentation. These mechanical effects are important in the retreat of scarps and the initial rapid loss of height in ramps, but are probably less important in debris fields and the distal portions of ramps because of the absence of free faces that lack mechanical support. The vermiform appearance of debris fields is similar to that of ramps, and seasonal changes in fields and ramps are similar but not identical, so the differences in processes appear to be in detail, not fundamentals.

The first implication of the observation of small scale topographic and albedo reversals is that any concept of backwasting comparable to that of the meters-high scarps is inapplicable to this relief. Backwasting of even small scarps of B unit materials generally proceeds at >2 m/♂y; some of the forms in Figs. 11 and 12 clearly do not change horizontally by >0.5 m over two, or even three Mars years, a factor of 10 less than might be predicted from changes in the larger scarps.

An unknown factor in the longevity of the debris field in the tapered part of the Tooth may be the wind-clearing processes responsible for hundreds of similar tapered windows into the PLD beneath B unit ice (Sec. 5.2; Fig. 7). For the Tooth, any influence of wind-clearing most probably is largely in the past: the possible source mesa has essentially disappeared before MY 24, and the width of area "Ta" has narrowed slightly after MY 12 (T2009, Fig. 15c), perhaps as a response to this shrinkage of the mesa. Because we do not know the mechanism of wind-clearing (enhanced loss or suppressed deposition), its effects on thin debris fields is unknown. We do know the dark exposure of the Tooth was largely unaffected by bright covering between MY 9 and MY 29. The shape of the tooth includes suggestions of scalloping typical of A0 mesas, but because those are subtle, the elongation dominates the shape. Shapes of the mesa developing reticulated terrain (Fig. 8) and of the debris area in Fig. S3 suggest the Tooth's shape may not be a unique

circumstance. Wind is also involved in the RSPC deposits in many different scales and settings, such as the topographically induced katabatic jumps that may lead to enhanced deposition along trough edges (Smith et al., 2015; Spiga and Smith, 2018). Wind can be effective in other polar environments at even larger scales on the PLD (Howard, 2000). Whatever the original role of the wind, the important factor is the survival of debris for >24 Mars years and the current very low downwasting rate that maintains a thin layer of debris.

7.3. Significance of debris

The debris is an alteration product of the relatively bright ice deposited on mesas and other surfaces in the RSPC. The alteration may arise from fracturing, changed configuration of included dust (concentration, particle orientations, particle surface properties), or other texture changes that strongly affect the photometric function. A possible compositional role still needs to be explored in detail (Calvin and Seelos, 2017). The debris does show that texture (small-scale topography), plays a role in loss and accumulation of CO_2 ice that plays a role in the cap's mass balance.

We have examined average and RSPC-wide characteristics as well as local examples of the debris, but there remains a vast trove of history to be found in individual sites and the geography of the debris. Part of this history is the meaning of the numerous remnants of A0 mesas recorded in the distinctively-shaped occurrences of debris fields: are these part of a steady-state, or do they record cap-wide changes? These distinctive relics, hundreds of m across, apparently owe their longevity to processes that effectively slow downwasting: the shuffling of new and older ice involved in repetitive relief inversions on single-meter scales.

The small scale relief inversions may provide a simple explanation for the large scale fossil relief inversions of A0 mesas. Because of the very low rate of downwasting of the debris, the surrounding areas can accumulate new residual ice relative to the height of the debris, and thus produce the large scale relief inversions observed across the RSPC (Fig. S11).

8. Summary

The retreat of scarps in the RSPC CO_2 ice leaves fractured debris, darker than undisturbed ice, divisible into "debris ramps" that are adjacent to mesas, and much larger "debris fields." Ramp widths and observed rates of scarp retreat indicate the ramp debris can survive for 10–20 Mars years. Debris fields arise by the merging of pits across a mesa, a geometrically different situation from scarp retreat around a mesa's perimeter, but which produces much the same materials and small scale features as in the ramps.

The small-scale topography within older and thinner portions of debris ramps and fields commonly inverts year-to-year. The presence of bright ice in this topography in late summer suggests the inversions may involve trapping winter ice in low areas, which likely retards average rate of loss of CO_2 ice and allows survival of thin debris coverings for 20 ♂y or even more in some areas.

Final loss of debris cover from some areas of PLD or PLD-like materials can initiate new net accumulation of CO_2 ice.

Calculated albedos of different materials in the RSPC using CTX data follow common seasonal trends until Ls 290–300°, after which rapid darkening of debris results from progressive exposure of darker, older CO_2 ice in the debris. The seasonal albedo trends correlate with specific morphologic milestones in the loss of seasonal ice observed in HiRISE data.

The longevity of thin debris covering may explain the formation of large-scale fossil inverted relief. The small-scale inversions, by reducing the effective vertical rate of erosion, may allow surrounding areas undergoing net accumulation to become higher than the areas of debris which occupy former relatively high mesas.

Acknowledgements

M. Wu, L. Posiolova, L. Saper T. Harrison, D. Shean, C. Brothers, A. Britton, G. Speth, and D. Susko targeted the south polar CTX images used in this study. We thank those who targeted and made available HiRISE data so helpful to this study. Further substantial help was provided by M. Caplinger, S. Davis, K. Edgett, K. Herkenhoff, P. Gierasch, M. Malin, T. Shannon, S. Sholes, and B. Thomas. We acknowledge the MRO and MSSS engineering and operations staff (past and present) for their hard work, who have contributed to the success of the CTX investigation. Funded in part by the Mars Reconnaissance Orbiter project, including subcontract 16-0689 to the University of Nevada Reno from Malin Space Science Systems. I. Smith and an anonymous reviewer get special thanks for unusually helpful reviews.

Data availability

Mars Reconnaissance Orbiter CTX images are archived at https://pds-imaging.jpl.nasa.gov/volumes/mro.html.HiRISE data are obtained from: https://www.uahirise.org/anazitisi.php.

Appendix A. Supplementary data

Supplementary data to this article can be found online at https://doi.org/10.1016/j.icarus.2020.113625.

References

Archinal, B.A., et al., 2011. Report of the IAU working group on cartographic coordinates and rotational elements: 2009. Celest. Mech. Dyn. Astron. 109, 101–135.
Batterson, C.M., Kahre, M.A., Haberle, R.M., Wilson, R.J., Kahanpaa, H., 2017. Secular Climate Change on Mars: An Update. AGU Fall Meeting Abstracts.
Becerra, P., Byrne, S., Brown, A.J., 2015. Transient bright "halos" on the south polar residual cap of Mars: implications for mass-balance. Icarus 251, 211–225.
Bierson, C.J., Phillips, R.J., Smith, I.B., Wood, S.E., Putzig, N.E., Nunes, D., Byrne, S., 2016. Stratigraphy and evolution of the buried CO_2 deposit in the Martian south polar cap. Geophys. Res. Lett. 43, 4172–4179.
Buhler, P.B., Ingersoll, A.P., Ehlmann, B.L., Fassett, C.I., Head, J.W., 2017. How the martian residual south polar cap develops quasi-circular and heart-shaped pits, troughs, and moats. Icarus 286, 69–93.
Buhler, P.B., Piqueux, S., Ingersoll, A.P., Ehlmann, B.L., Hayne, P.O., 2019. The co-evolution of mars' atmosphere and massive south polar CO_2 ice deposit. LPI Contributions 2089, 6008.
Byrne, S., Ingersoll, A.P., 2003a. Martian climatic events on timescales of centuries: evidence from feature morphology in the residual south polar ice cap. Geophys. Res. Lett. 30, 130000–130001.
Byrne, S., Ingersoll, A.P., 2003b. A sublimation model for Martian south polar ice features. Science 299, 1051–1053.
Byrne, S., et al., 2008. Explaining the persistence of the southern residual cap of Mars: HiRISE data and landscape evolution models. Lunar Planet. Sci. 39 (Abstract 2252).
Calvin, W.M., Seelos, K.D., 2017. Compositional Variation of the Icy Units of the South Residual Polar Cap of Mars Using CRISM. 48th LPSC, Abstract #1604.
Chinnery, H.E., Hagermann, A., Kaufmann, E., Lewis, S.R., 2018. The penetration of solar radiation into carbon dioxide ice. Journal of Geophysical Research (Planets) 123, 864–871.
Chinnery, H.E., Hagermann, A., Kaufmann, E., Lewis, S.R., 2019. The penetration of solar radiation into water and carbon dioxide snow, with reference to Mars. Journal of Geophysical Research (Planets) 124, 337–348.
Clancy, R.T., et al., 2000. An intercomparison of ground-based millimeter, MGS TES, and Viking atmospheric temperature measurements: seasonal and interannual variability of temperatures and dust loading in the global Mars atmosphere. J. Geophys. Res. 105, 9553–9572.
Douté, S., Schmitt, B., Langevin, Y., Bibring, J.P., Altieri, F., Bellucci, G., Gondet, B., Poulet, F., 2007. South Pole of Mars: nature and composition of the icy terrains from Mars express OMEGA observations. Planetary and Space Science 55 (1–2), 113–133.
Greeley, R., Iverson, J.D., 1985. Wind as a Geologic Process on Earth, Mars, Venus, and Titan. Cambridge Univ. Pr4ess, Cambridge.
Haberle, R.M., Kahre, M.A., 2010. Detecting secular climate change on Mars. International Journal of Mars Science and Exploration 5, 68–75.
Haberle, R.M., et al., 2014. Secular climate change on Mars: an update using one Mars year of MSL pressure data. In: AGU Fall Meeting Abstracts 3947.
Hansen, C.J., et al., 2010. HiRISE observations of gas sublimation-driven activity in Mars' southern polar regions: I. Erosion of the surface. Icarus 205, 283–295.
Hayne, P.O., Paige, D.A., Schofield, J.T., Kass, D.M., Kleinbohl, A., Heavens, N.G., McCleese, D.J., 2012. Carbon dioxide snow clouds on Mars: south polar winter observations by the Mars Climate Sounder. Journal of Geophysical Research (Planets) 117, E08014.

Hayne, P.O., Paige, D.A., Heavens, N.G., 2014. The role of snowfall in forming the seasonal ice caps of Mars: models and constraints from the Mars Climate Sounder. Icarus 231, 122–130.
Howard, A.D., 2000. The role of Eolian processes in forming surface features of the Martian polar layered deposits. Icarus 144, 267–288.
Iversen, J.D., Greeley, R., 1984. Martian crater dark streak lengths: explanation from wind tunnel experiments. Icarus 58, 358–362.
James, P.B., Bonev, B.P., 2008. Effect of atmospheric dust on interannual variability in the Martian south polar cap. In: Third International Workshop on the Mars Atmosphere: Modeling and Observations 9051.
James, P.B., Kieffer, H.H., Paige, D.A., 1992. In: Kieffer, H.H., Jakosky, B.M., Snyder, C. W., Mathews, M.S. (Eds.), The seasonal cycle of carbon dioxide on Mars, in Mars. Univ. of Arizona Press, Tucson, pp. 934–968.
James, P.B., Thomas, P.C., Wolff, M.J., Bonev, B.P., 2007. MOC observations of four Mars year variations in the south polar residual cap of Mars. Icarus 192, 318–326.
James, P.B., Thomas, P.C., Calvin, W.M., Haberle, R., 2009. CTX observations of seasonal albedo variations in the. In: "Tooth Region" of the RSPC. Third International Workshop on Mars Polar Energy Balance and the CO_2 Cycle, 25.
James, P.B., Thomas, P.C., Malin, M.C., 2010. Variability of the south polar cap of Mars in Mars years 28 and 29. Icarus 208, 82–85.
Kahre, M.A., Haberle, R.M., 2010. Mars CO_2 cycle: effects of airborne dust and polar cap ice emissivity. Icarus 207, 648–653.
Kieffer, H.H., 2003. Behavior of solid CO_2 on Mars: a real zoo. In: Sixth International Conference on Mars 3158.
Kieffer, H.H., Titus, T.N., Mullins, K.F., Christensen, P.R., 2000. Mars south polar spring and summer behavior observed by TES: seasonal cap evolution controlled by frost grain size. J. Geophys. Res. 105, 9653–9699. https://doi.org/10.1029/1999JE001136.
Kieffer, H.H., Christensen, P.R., Titus, T.N., 2006. CO_2 jets formed by sublimation beneath translucent slab ice in Mars' seasonal south polar ice cap. Nature 442, 793–796.
Langevin, Y., et al., 2007. Observations of the south seasonal cap of Mars during recession in 2004–2006 by the OMEGA visible/near-infrared imaging spectrometer on board Mars express. Journal of Geophysical Research (Planets) 112, E08S12.
Lee, S.W., 1984. Mars: wind streak production as related to obstacle type and size. Icarus 58, 339–357.
Line, M.R., Ingersoll, A.P., 2010. Can the solid state greenhouse effect produce ~100 year cycles in the Mars south polar residual CO_2 ice cap?. In: AGU Fall Meeting Abstracts 2010, pp. P53F–P507.
Malin, M.C., Danielson, G.E., Ingersoll, A.P., Masursky, H., Veverka, J., Ravine, M.A., Soulanille, T.A., 1992. Mars Observer camera. J. Geophys. Res. 97, 7699–7718.
Malin, M.C., Caplinger, M.A., Davis, S.D., 2001. Observational evidence for an active surface reservoir of solid carbon dioxide on Mars. Science 294, 2146–2148.
Malin, M.C., et al., 2007. Context camera investigation on board the Mars Reconnaissance Orbiter. Journal of Geophysical Research (Planets) 112, E05S04.
McEwen, A.S., et al., 2007. Mars Reconnaissance Orbiter's high resolution imaging science experiment (HiRISE). Journal of Geophysical Research (Planets) 112, E05S02. https://doi.org/10.1029/2005JE002605.
Moore, J.M., Wilhelms, D.E., 2001. Hellas as a possible site of ancient ice-covered lakes on Mars. Icarus 154, 258–276.
Morgan, A.M., et al., 2014. Sedimentology and climatic environment of alluvial fans in the martian Saheki crater and a comparison with terrestrial fans in the Atacama Desert. Icarus 229, 131–156.
Murray, B.C., Malin, M.C., 1973. Polar volatiles on Mars-theory versus observation. Science 182, 437–443.
Paige, D.A., Ingersoll, A.P., 1985. Annual heat balance of Martian polar caps: Viking observations. Science 228, 1160–1168.
Pain, C.F., Ollier, C.D., 1995. Inversion of relief - a component of landscape evolution. Geomorphology 12 (2), 151–165.
Pathare, A., Ingersoll, A., Titus, T., Byrne, S., 2005. Pitting within the Martian south polar residual cap: evidence for pressurized subsurface carbon dioxide. In: AGU Fall Meeting Abstracts A198.
Phillips, R.J., et al., 2011. Massive CO_2 ice deposits sequestered in the south polar layered deposits of Mars. Science 332, 838841.
Piqueux, S., Christensen, P.R., 2008a. Deposition of CO_2 and erosion of the Martian south perennial cap between 1972 and 2004: implications for current climate change. Journal of Geophysical Research (Planets) 113, E02006. https://doi.org/10.1029/2007JE002969.
Piqueux, S., Christensen, P.R., 2008b. North and south subice gas flow and venting of the seasonal caps of Mars: a major geomorphological agent. Journal of Geophysical Research (Planets) 113, E06005.
Piqueux, S., Edwards, C.S., Christensen, P.R., 2008. Distribution of the ices exposed near the south pole of Mars using Thermal Emission Imaging System (THEMIS) temperature measurements. Journal of Geophysical Research (Planets) 113, E08014.
Piqueux, S., Byrne, S., Kieffer, H.H., Titus, T.N., Hansen, C.J., 2015. Enumeration of Mars years and seasons since the beginning of telescopic exploration. Icarus 251, 332–338.
Portyankina, G., Markiewicz, W.J., Thomas, N., Hansen, C.J., Milazzo, M., 2010. HiRISE observations of gas sublimation-driven activity in Mars southern polar regions: III. Models of processes involving translucent ice. Icarus 205, 311–320.
Putzig, N.E., Smith, I.B., Perry, M.R., Foss II, F.J., Campbell, B.A., Phillips, R.J., Seu, R., 2018. Three-dimensional radar imaging of structures and craters in the Martian polar caps. Icarus 308, 138–147.
Smith, D., Neumann, G., Arvidson, R.E., Guinness, E.A., Slavney, S., 2003. Mars Global Surveyor Laser Altimeter Mission Experiment Gridded Data Record. NASA Planetary Data System (MGS-M-MOLA-5-MEGDR-L3-V1.0).
Smith, I.B., Spiga, A., Holt, J.W., 2015. Aeolian processes as drivers of landform evolution at the South Pole of Mars. Geomorphology 240, 54–69.
Spiga, A., Smith, I., 2018. Katabatic jumps in the Martian northern polar regions. Icarus 308, 197.
Tanaka, K.L., Kolb, E.J., Fortezzo, C., 2007. Recent Advances in the Stratigraphy of the Polar Regions of Mars. LPI Contributions 1353, p. 3276.
Thomas, P., Veverka, J., Gineris, D., Wong, L., 1984. 'Dust' streaks on Mars. Icarus 60, 161–179.
Thomas, P.C., et al., 2000. North-south geological differences between the residual polar caps on Mars. Nature 404, 161–164.
Thomas, P.C., Malin, M.C., James, P.B., Cantor, B.A., Williams, R.M.E., Gierasch, P., 2005. South polar residual cap of Mars: features, stratigraphy, and changes. Icarus 174, 535–559.
Thomas, P.C., James, P.B., Calvin, W.M., Haberle, R., Malin, M.C., 2009. Residual south polar cap of Mars: stratigraphy, history, and implications of recent changes. Icarus 203, 352–375.
Thomas, P.C., Calvin, W.M., Gierasch, P., Haberle, R., James, P.B., Sholes, S., 2013. Time scales of erosion and deposition recorded in the residual south polar cap of Mars. Icarus 225, 923–932.
Thomas, P.C., Calvin, W., Cantor, B., Haberle, R., James, P.B., Lee, S.W., 2016. Mass balance of Mars' residual south polar cap from CTX images and other data. Icarus 268, 118–130.
Veverka, J., Gierasch, P., Thomas, P., 1981. Wind streaks on Mars: meteorological control of occurence and mode of formation. Icarus 45, 154–166.
Williams, R.M.E., Irwin, R.P., Zimbelman, J.R., 2009. Evaluation of paleohydrologic models for terrestrial inverted channels: implications for application to Martian sinuous ridges. Geomorphology 107, 300–315.